Author/s:
Tino, RB;Yeo, AU;Brandt, M;Leary, M;Kron, T

Title:
A customizable anthropomorphic phantom for dosimetric verification of 3D-printed lung, tissue, and bone density materials

Date:
2022-01-01

Citation:
Tino, R. B., Yeo, A. U., Brandt, M., Leary, M. & Kron, T. (2022). A customizable anthropomorphic phantom for dosimetric verification of 3D-printed lung, tissue, and bone density materials. Medical Physics, 49 (1), pp.52-69. https://doi.org/10.1002/mp.15364.

A customizable anthropomorphic phantom for dosimetric verification of 3D-printed lung, tissue, and bone density materials

Rance Bolislis Tino[1,3,5], Adam Unjin Yeo[2,3], Milan Brandt[1,5], Martin Leary[1,5] and Tomas Kron (corr-auth)[3,4,5,6†]

[1] *RMIT Centre for Additive Manufacturing, School of Engineering, RMIT University, Melbourne, VIC 3001, Australia*

[2] *School of Applied Sciences, RMIT University, Melbourne, VIC 3001, Australia*

[3] *Peter MacCallum Cancer Centre, Department of Physical Sciences, Melbourne, VIC 3000, Australia*

[4] *Sir Peter MacCallum Department of Oncology, University of Melbourne, Melbourne, VIC 3010, Australia*

[5] *ARC Industrial Transformation Training Centre in Additive Biomanufacturing, Queensland University of Technology, Brisbane, QLD 4059, Australia*

[6] *Centre for Medical Radiation Physics, University of Wollongong, Wollongong, NSW 2500, Australia*

Abstract

Purpose: To design and manufacture a customized thoracic phantom slab utilizing the 3D printing process, also known as Additive Manufacturing (AM), consisting of different tissue density materials. Here, we demonstrate the 3D printed phantom's clinical feasibility for imaging and dosimetric verification of Volumetric Modulated Arc Radiotherapy (VMAT) plans for lung and spine Stereotactic Ablative Body Radiotherapy (SABR) through end-to-end dosimetric verification.

Methods: A customizable anthropomorphic phantom slab was designed using the CT dataset of a commercial phantom (adult female ATOM® dosimetry phantom, CIRS Inc., USA). Material extrusion 3D printing was utilized to manufacture the phantom slab consisting of acrylonitrile butadiene styrene material for lung and the associated lesion, polylactic acid material for soft-tissue and spinal cord, and both polylactic acid and iron-reinforced polylactic acid materials for bone. CT images were acquired for both the commercial phantom and 3D printed phantom for HU comparison. VMAT plans were generated for spine and lung SABR scenarios and were delivered as per departmental SABR protocols using a Varian TrueBeam™ STx linear accelerator. End-to-end dosimetry was implemented with radiochromic films, analyzed with gamma criteria of 5% dose difference and a distance to agreement of 1 mm, at a 10% low-dose threshold by comparing with calculated dose using the Acuros (AXB) algorithm of the Eclipse Treatment planning system (v15.6).

Results: 3D printed phantom inserts were observed to produce HU ranging from -750 to 2100. The 3D printed phantom slab was observed to achieve a similar range of HU from the commercial phantom including a mean HU of -760 for lung tissue, a mean HU of 50 for soft tissue, and a mean HU of 220 and 630 for low- and high-density bone, respectively. Film dosimetry results show 2D-gamma passing rates for lung SABR (internal and superior) and for spine SABR (inferior and superior) over 98% and 90%, respectively.

Conclusions: The end-to-end testing of VMAT plans for spine and lung SABR suggests the clinical feasibility of the 3D printed phantom, consisting of different tissue density materials that emulate lung, soft-tissue, and bone in kV imaging and MV photon dosimetry. Further investigation of the proposed 3D printing techniques for manufacturability and reproducibility will enable the development of clinical 3D printed phantoms in radiotherapy.

Key words: anthropomorphic phantoms, personalized 3D-printing, tissue-equivalence, treatment verification, dosimetry, radiotherapy, end-to-end testing

†Corresponding author. E-mail: Tomas.Kron@petermac.org, Mailing: Petermac Peter MacCallum Cancer Centre, Department of Physical Sciences, VCCC, 305 Grattan Street, Melbourne VIC 3000, Australia

1 Introduction

Advancing radiotherapy technologies increase the demand for complex and personalized treatment plans. Consequently, highly advanced radiotherapy treatments create the need for added accuracy and flexibility (in shape and tissue densities) in the current state-of-the-art anthropomorphic phantoms. Researchers and clinicians utilize phantoms in the acceptance, commissioning, and routine quality assurance (QA) of diagnostic and treatment systems and the regulation of clinical trials.[1, 2] However, commercial phantoms are limited to models consisting of homogeneous tissue densities using standard human dimensions[3-7] and are incapable of mimicking tissue imaging characteristics for different human organs[1], let alone various pathological changes. In recent times, Ehler *et al.* established the process of manufacturing a patient-specific head phantom for treatment verifications and QA using a low-cost Additive Manufacturing (AM) or 3D printing technology called Material Extrusion (MEX), which is commonly known as fused deposition modelling or fused filament fabrication. The researchers demonstrated the low-cost and personalized manufacturing of anthropomorphic phantoms, however, it is limited to emulating only soft-tissue densities.[8] Since then, extensive research on MEX printing materials has been conducted to quantify their radiological properties to emulate other range of tissue densities including bone and lung.[9] Here, the advancement of 3D printing technologies continues with a substantial pace as researchers further explore novel MEX printing techniques to attain enhanced tissue equivalence in terms of the material's CT attenuation (HU) and absorbed dose (Gy) for a given energy range.[10-13]

Early efforts by Yoon *et al.* demonstrated the use of a motion phantom with a lung rod insert manufactured with MEX printing using a Polylactic Acid (PLA) filament.[14] The 3D printed lung rod insert consist of a patient-specific lesion and was utilized with a motion phantom to verify dose distributions in a more realistic respiratory condition. This concept was found to be clinically feasible for assessing the accuracy of a lung tracking system[15] and the investigation of various patient-specific lung lesion sizes and positions comparing dose measuring algorithms using Stereotactic Ablative Body Radiotherapy (SABR) for 3D conformal[16] or Volumetric Modulated Arc Therapy (VMAT)[17, 18] treatment planning. Another area of research involves using non-printable materials, known as tissue-substitutes, combined with 3D printing materials to enhance the emulation of tissue HU in addition to a mobile tumor, allowing a more realistic replication of lung density and deformation.[19] Despite promising outcomes of MEX printed anthropomorphic phantoms in the dosimetry domain, recurring limitations found in the current literature—the lack of quantifiable data in the reported HU for the materials used due to the existing inter- and intra-variability caused by different printing materials, settings and machine systems; the limited range of achieved HU in the attempt to emulate lung-, soft-, and bone-tissue in the CT imaging domain; and, the lack of a customizable phantom design which may allow for the assessments of multiple patient-specific lesions at various sizes and positions. It is also essential

to consider that the HU of a MEX printing material identical to that of any tissue densities does not necessarily correlate to dose attenuations, and it depends entirely on the material's atomic composition. Quantifying this difference is a critical factor for further calibrations through treatment planning and dose measurements when considering patient-specific pathological features for personalized dosimetry.

At present, MEX printing techniques to manufacture a phantom commonly use the *indirect* manufacturing process, which utilizes 3D printing materials combined with tissue-substitutes. In contrast, the *direct* manufacturing process only uses 3D printing materials.[16, 18, 20] The *indirect* manufacturing process uses specialized materials, leading to an increase in material and manufacturing costs—the required manual process for producing the tissue-substitute if a specific density range is preferred, often limited to emulating a narrow range of tissue densities, and the use of standard MEX printing parameters inhibiting the accurate replication of internal tissue geometries. In response to these challenges, this work integrates and implements the reported 3D printing techniques utilizing the *direct* additive manufacturing process to emulate different tissue densities for lung, soft-tissue, and bone[21, 22] and establish a proof-of-concept for 3D printed customizable phantoms for dosimetric verification studies. As such, this study aims i) to develop a 3D printed, low-cost, customizable anthropomorphic thoracic phantom slab to allow for the insertion of patient-specific lesions, and ii) to implement the 3D printed phantom for the end-to-end testing of VMAT treatment plans for spine and lung SABR scenarios and demonstrate its clinical feasibility for radiotherapy applications.

2 Materials and Methods

Preliminary work in this research involved the fabrication of phantom inserts designed to fit an Electron Density (ED) mini phantom. CT imaging and electron density assessments were implemented for lung, soft-tissue, and bone density materials.

A commercially available phantom (adult female ATOM® dosimetry phantom, CIRS, Inc., USA) was utilized as the clinically accepted reference model for the 3D printed anthropomorphic phantom slab. The commercial phantom was scanned at a CT energy of 140 kVp (2 mm slice thickness and increments) using a fan beam CT imaging scanner (Philips Brilliance Big Bore CT). The phantom slab of interest was manually contoured to generate a volume of interest (VOI) and was observed with a mean HU of -754 ± 82 for lung tissue, 723 ± 48 for high-density bone, for 85 ± 22 for low-density bone, 23 ± 19 for soft tissue, and 65 ± 26 for the spinal cord. These HU values were used as a reference in selecting the required lung, soft-tissue, and bone density materials for generating the 3D model of the phantom slab. Finally, the 3D printed phantom was implemented to validate and verify the developed VMAT plans for a spine and lung SABR using radiochromic film measurements. Design and development workflows for the 3D printed phantom are illustrated in Figure 1.

2.1 Soft-tissue and Bone density materials

A previous study has demonstrated the production of bone-equivalent densities using the interlace deposition method of iron reinforced PLA (Fe-PLA) filament (ρ = 1.85 g/cm^3, Proto-Pasta, US) and PLA (ρ =

1.25 g/cm^3, Raise3D, US). The interlace deposition method utilizes the material layer thickness ratio, V_{ratio}, of Fe-PLA and PLA to achieve a specific range of mean HU at a particular CT energy[22].

A total of five interlace deposition phantom ED inserts were manufactured using a commercially available dual-extrusion printer (Raise3D Pro 2, Raise3D, USA), including an insert with: a V_{ratio} of 0.0 corresponding to solid PLA; a V_{ratio} of 0.50 corresponding to a layer thickness of 0.2 mm for PLA and Fe-PLA; a V_{ratio} of 0.33, corresponding to a PLA layer thickness of 0.4 mm and a Fe-PLA layer thickness of 0.2 mm; a V_{ratio} of 0.11, corresponding to a layer thickness of 1.6 mm for PLA and 0.2 mm for Fe-PLA; and a V_{ratio} of 1.0 for a solid Fe-PLA insert. For printing, the left extruder uses a nozzle diameter of 0.8 mm to extrude the Fe-PLA filament at 210°C, and the right extruder uses a nozzle diameter of 0.4 mm to extrude the PLA filament at 205°C. A printing layer height of 0.2 mm was utilized with retraction settings for the PLA filament to avoid the extrusion of unnecessary materials during printing. Retraction settings were disabled for the Fe-PLA filament to prevent nozzle clogging due to the abrasive nature of the iron particle content.

2.2 Lung density material

Gyroid structures[21] were utilized to emulate the varying densities of lung tissue using Acrylonitrile Butadiene Styrene (ABS) filament. Gyroid structures were parameterized at varying periodicity, *P*, which defines the unit cell size at x, y, and z directions and wall thickness, *t,* defining the total distance of gyroid offset surfaces in 3D space. For preliminary assessments, CT imaging was conducted to investigate fifteen gyroid phantom ED inserts, including five control factor levels for *P* (3 mm, 4 mm, 5 mm, 6 mm, 7 mm), and three levels of *t* (0.6 mm, 1 mm, 1.4 mm) using ABS filament (ρ = 1.10-1.15 g/cm^3, Raise3D, US). An additional phantom ED insert was manufactured using only ABS at 100% infilling. A total of sixteen ABS phantom inserts were manufactured using the same printer utilized in the previous section, with a nozzle size of 0.4 mm, a nozzle temperature of 255°C and a layer height of 0.2 mm.

After printing and post-processing (manual removal of unnecessary materials on the specimen's surface), CT imaging was implemented for all printed phantom ED inserts (interlace deposition of PLA and Fe-PLA insert and ABS gyroids inserts) placed inside the existing ED mini phantom. The CT imaging protocol includes three clinically used beam qualities (140 kVp, 120 kVp, 80 kVp) with CT parameters including a slice thickness and increments of 2 mm, a collimation of 16x0.75 mm, an iDose^4 iterative reconstruction with Standard B filter and DoseRight tool (level 4), a default current value of 218 mAs and a default CTDIvol of 8.6 mGy. CT data were imported to Varian Eclipse v15.6 treatment planning system (TPS) for contouring to extract material mean HU (± one standard deviation) within the specified VOI, mass density, ρ_m and relative electron density, $\rho_{e/w}$. Results were compared to the commercially available phantom ED inserts.

2.3 Design and manufacture of anthropomorphic phantom

Figure 1 below illustrates the design and printing workflow of the 3D printed phantom from reference model generation to applying various MEX 3D printing techniques for tissue density emulation. This is followed by the manufacturing process of the 3D printed phantom from model slicing to printing.

An open-source software (3Dslicer, USA) was utilized to segment the tissues from the commercial CIRS phantom CT dataset using its global Otsu threshold function. Here, using a tessellation function (marching cube algorithm) in the software, 3D models of the segmented tissues were generated with a smoothing factor of 0.4. Figure 1: Design and printing workflow of an anthropomorphic phantom. 1.) generation of phantom slab 3D model, 2.) virtual post-processing of the phantom slab 3D model, 3.) application of the proposed MEX 3D printing techniques to emulate lung-, soft-, and bone-tissue densities, 4.) slicing of the phantom slab 3D model and 5.) gyroid lung sub-sections using IdeaMaker software, 6.) printing of the phantom slab and gyroid lung sub-section 3D models.

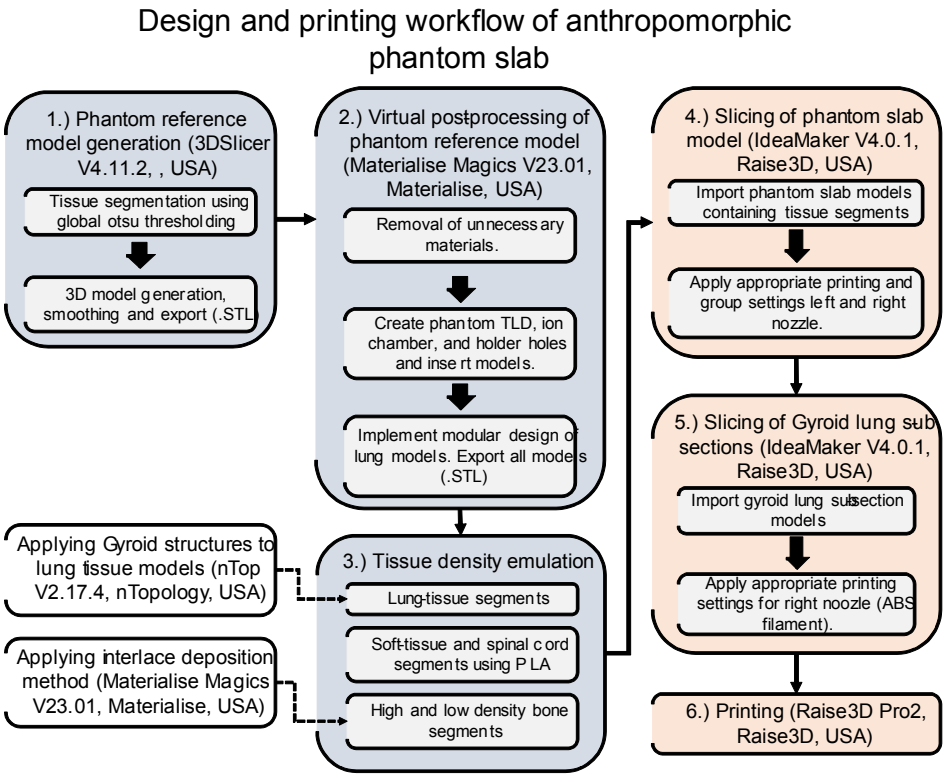

Figure 2a shows the selected phantom slab of interest consisting of soft tissue, homogeneous high- and low-density bone, spinal cord, and lung tissue segments. A computer aided design processing software was further utilized (Magics, Materialise) to remove unnecessary triangles and shells from the generated 3D models. Here, Thermoluminiscent Dosimeter (TLD), ion chamber, and holder insertion holes were generated with a clearance of 0.5 mm for generated inserts (see Figure 1: Design and printing workflow of an anthropomorphic phantom. 1.) generation of phantom slab 3D model, 2.) virtual post-processing of the phantom slab 3D model, 3.) application of the proposed MEX 3D printing techniques to emulate lung-, soft-, and bone-tissue densities, 4.) slicing of the phantom slab 3D model and 5.) gyroid lung sub-sections using IdeaMaker software, 6.) printing of the phantom slab and gyroid lung sub-section 3D models.

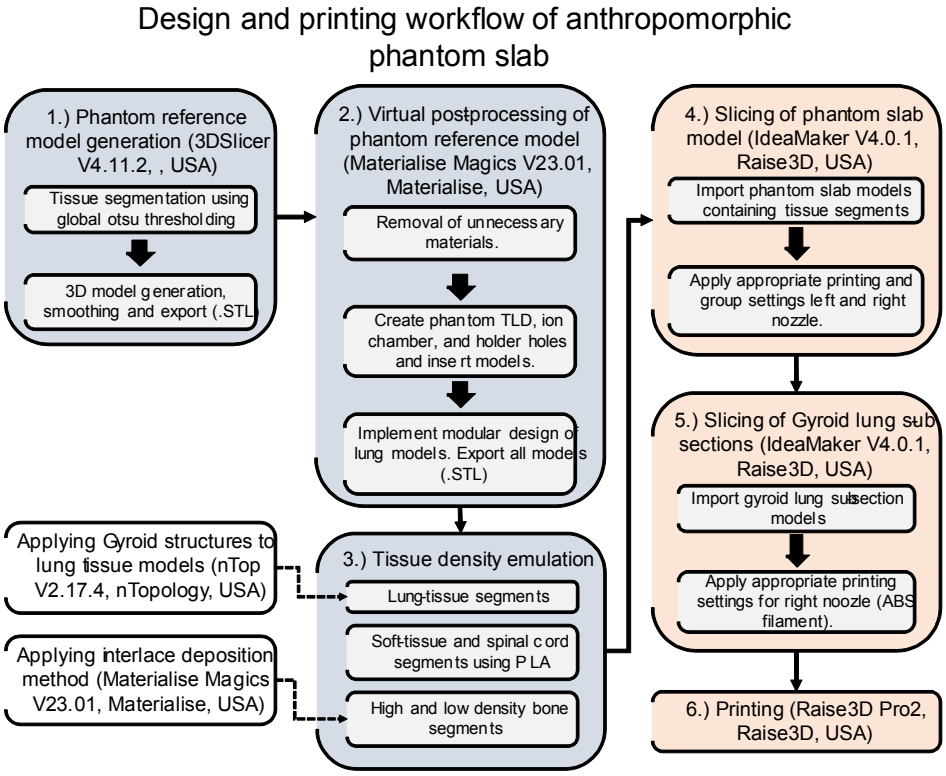

Figure 2b). Furthermore, segmented lung models were virtually cut into a total of 14 sub-sections (R1-R7 and L1-L7) to allow a modular design and the assessment of a patient-specific NSCLC lesion (see Figure 1: Design and printing workflow of an anthropomorphic phantom. 1.) generation of phantom slab 3D model, 2.) virtual post-processing of the phantom slab 3D model, 3.) application of the proposed MEX 3D printing techniques to emulate lung-, soft-, and bone-tissue densities, 4.) slicing of the phantom slab 3D model and 5.) gyroid lung sub-sections using IdeaMaker software, 6.) printing of the phantom slab and gyroid lung sub-section 3D models.

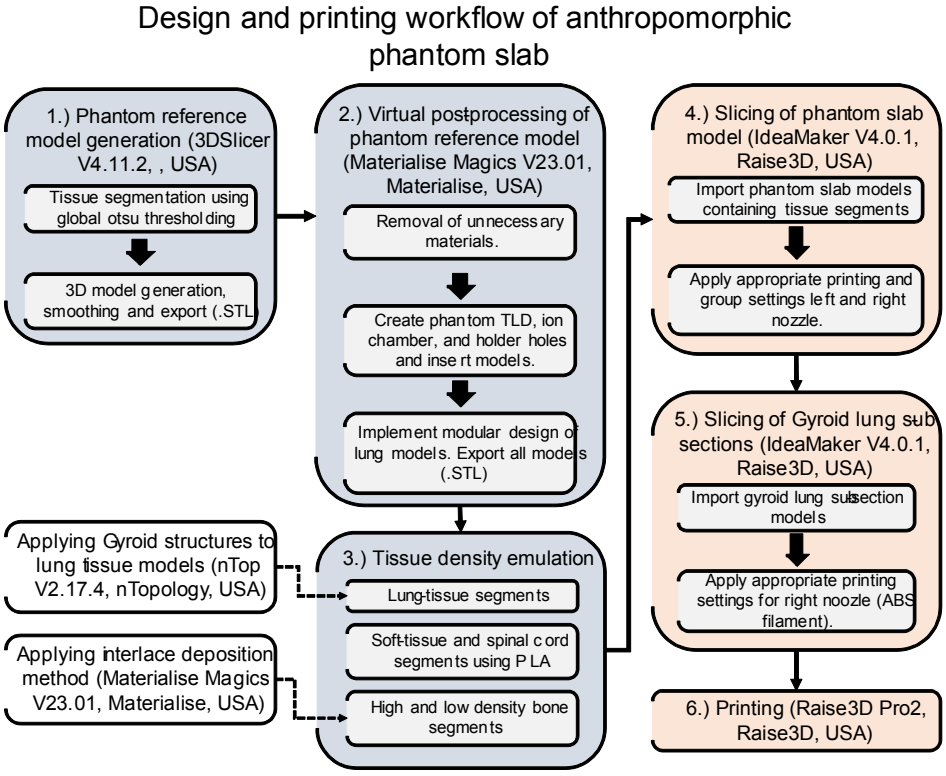

Figure 2c). Due to the known toolpath complexity of 3D printing gyroid structures, in addition to the thin wall thickness used, surface roughness and shape inaccuracy were observed.[21] The virtual cutting process involves the removal of 0.4 mm material from the boundary regions of the gyroid lung sub-sections excluding their interaction surface with the phantom slab. This spacing allows for the smooth insertion of the sub-sections without compromising structural integrity of the surrounding sub-sections.

Gyroid lung models were generated using the segmented lung 3D models (nTopology, USA). First, the left and right lung-tissue models were imported in the nTopology software where a 'Walled TPMS' structure was generated within the imported lung models with parameters containing a *P* of 5 mm, a *t* of 0.6 mm, and a fill type of 'Gyroid'. The resulting gyroid lung models had to be converted back to a mesh model using a resurfacing function, enabling the models to be exported as .STL files for printing. A small spiculated NSCLC lesion with a cavity was chosen from the NSCLC-Radiomics dataset (LUNG1_061, The Cancer Imaging Archive (TCIA))[23]. The lesion was further segmented and processed using 3DSlicer software to generate its associated 3D model (see Figure 1: Design and printing workflow of an anthropomorphic phantom. 1.) generation of phantom slab 3D model, 2.) virtual post-processing of the phantom slab 3D model, 3.) application of the proposed MEX 3D printing techniques to emulate lung-, soft-, and bone-tissue densities, 4.) slicing of the phantom slab 3D model and 5.) gyroid lung sub-sections using IdeaMaker software, 6.) printing of the phantom slab and gyroid lung sub-section 3D models.

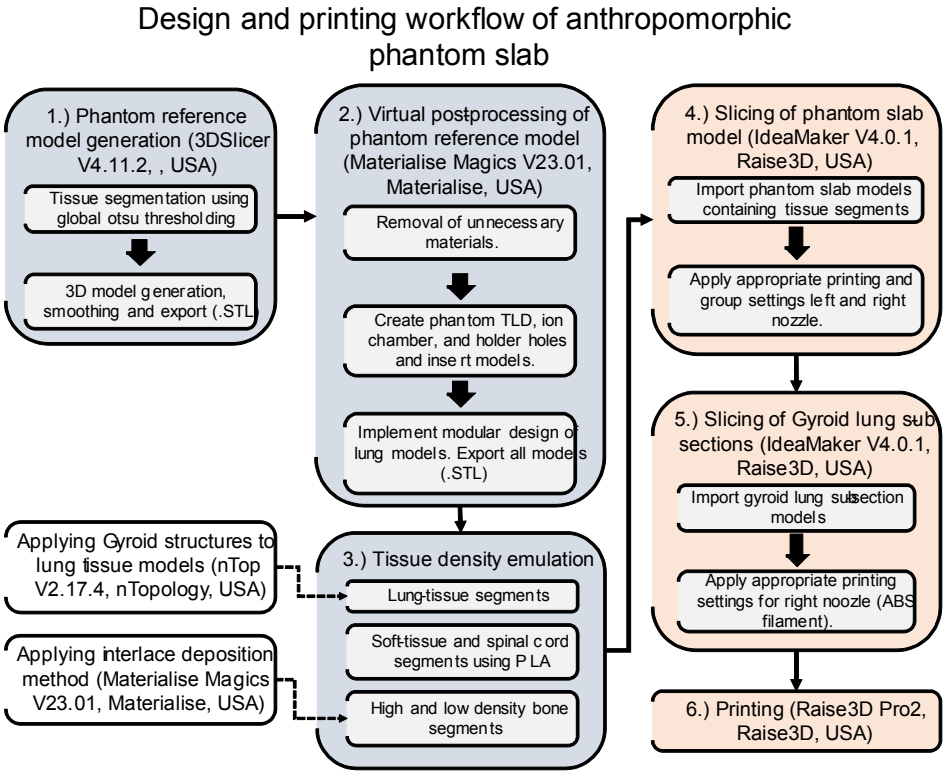

Figure 2: Segmentation and generation process of the adult CIRS ATOM phantom slab from CT for 3D printing. (a) CT of CIRS ATOM® adult phantom, (b) generated 3D phantom model with dosimetry insertion holes including holder holes for stability, TLD holders, and an ion chamber hole, (c) tissue segments including a spinal cord, high- and low- density bone, soft tissue, and lung tissue sub-sections (L1-L7 and R1-R7).

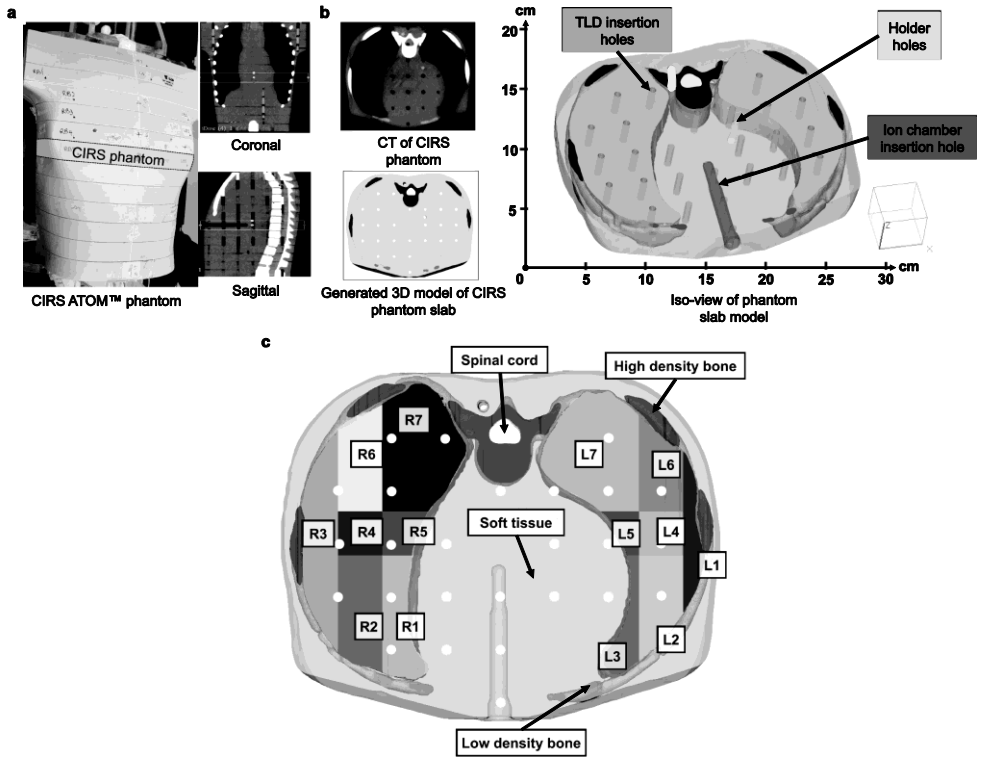

Figure 3). Lung gyroid sub-sections with the lesion model were combined utilising Magic's Boolean functions (Magics, Materialise) and were printed using ABS filament (ρ = 1.10-1.15 g/cm^3, Raise3D, US) with a nozzle diameter of 0.4 mm at 100% infilling.

Dual-extrusion printing was utilized to manufacture the phantom slab model consisting of the high- and low-density bone, soft-tissue, and spinal cord segments. The high- and low-density bone segments were printed using the interlace deposition method with a V_{ratio} of 0.33, and 0.11, respectively. A PLA filament (ρ =

1.25 g/cm^3, Raise3D, US) was used for soft-tissue and spinal cord segments at 100% infill (see

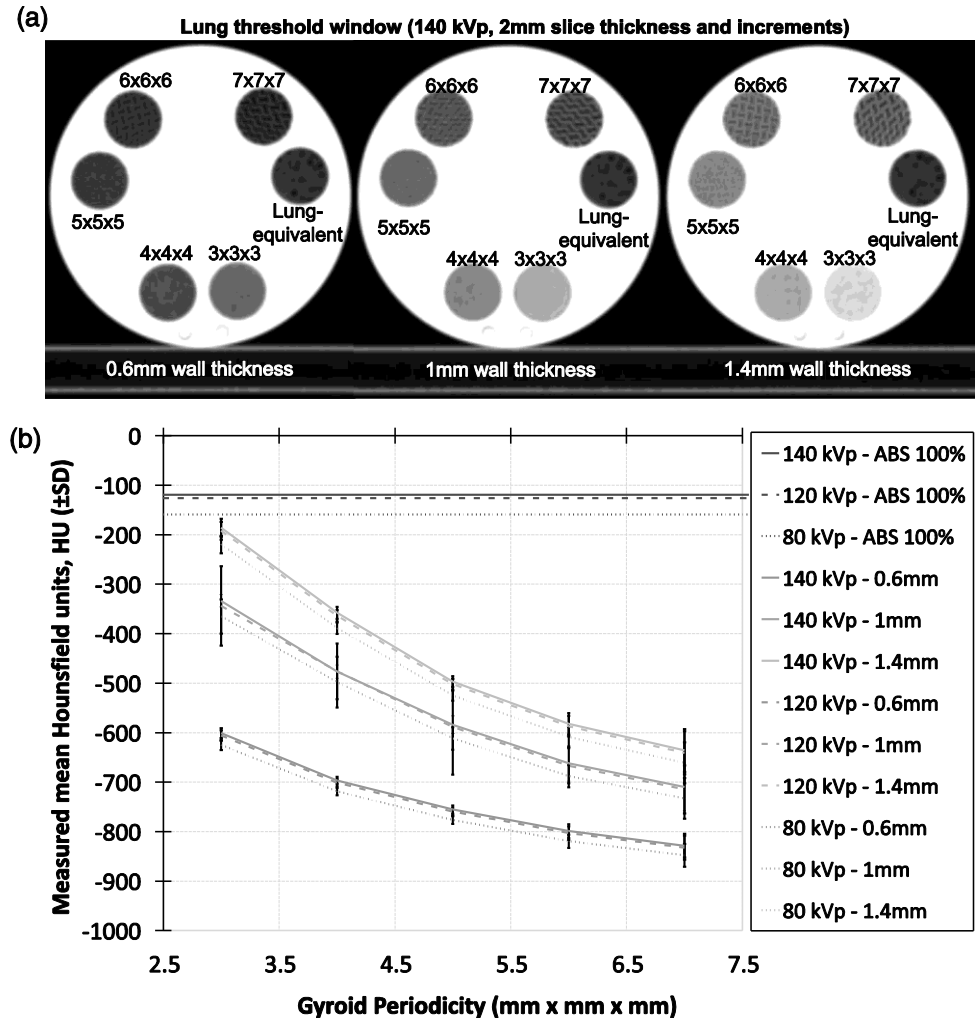

Figure 11: Generated volume structures for lesion and gyroid lung for samples 1, 2 and 3 (140 kVp, 2/2 sagittal view).

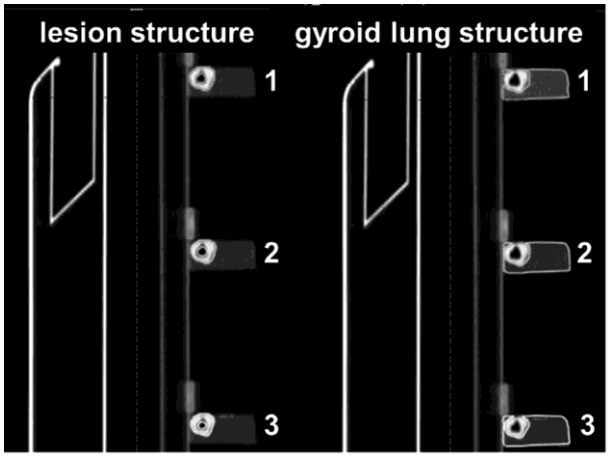

Figure 12: Generated horizontal HU line profiles from registered dataset containing samples 1, 2 and 3 (140 kVp 2/2, frontal, sagittal, and transversal planes).

for an overview of the printing settings utilized for the tissue segments).

To evaluate the HU reproducibility of 3D printing for extreme cases (complex 3D printing toolpaths), we printed three identical samples of the gyroid lung sub-section, L7, containing a lesion on separate occasions, and were scanned using a fan beam CT with varying kV energies at 2 mm slice thickness (Philips Brilliance Big Bore CT). Contours (VOI) were generated using auto-thresholding for the 3D printed identical samples, where extracted mean HU (± one standard deviation) were compared among the three. Samples were further compared by using generated HU line profiles across frontal, sagittal and transversal planes (see Appendix B).

2.4 SABR End-to-end testing of anthropomorphic phantom

End-to-end testing from simulation to measurement analysis was performed according to the departmental SABR clinical protocol (see Figure 1: Design and printing workflow of an anthropomorphic phantom. 1.) generation of phantom slab 3D model, 2.) virtual post-processing of the phantom slab 3D model, 3.) application of the proposed MEX 3D printing techniques to emulate lung-, soft-, and bone-tissue densities, 4.) slicing of the phantom slab 3D model and 5.) gyroid lung sub-sections using IdeaMaker software, 6.) printing of the phantom slab and gyroid lung sub-section 3D models.

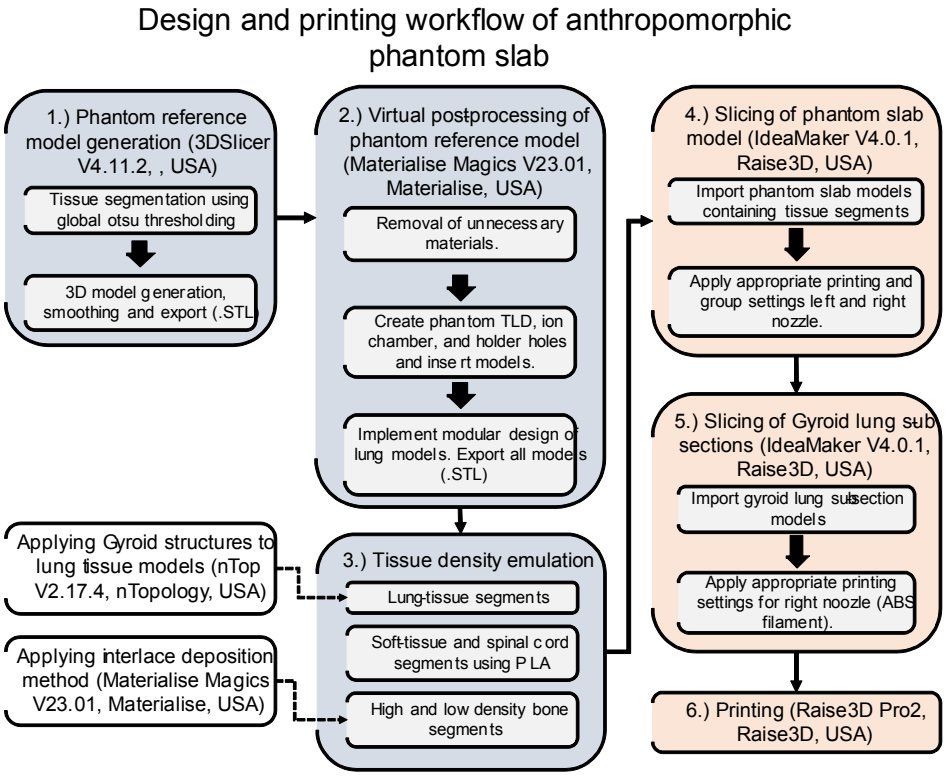

Figure 2: Segmentation and generation process of the adult CIRS ATOM phantom slab from CT for 3D printing. (a) CT of CIRS ATOM® adult phantom, (b) generated 3D phantom model with dosimetry insertion holes including holder holes for stability, TLD holders, and an ion chamber hole, (c) tissue segments including a spinal cord, high- and low- density bone, soft tissue, and lung tissue sub-sections (L1-L7 and R1-R7).

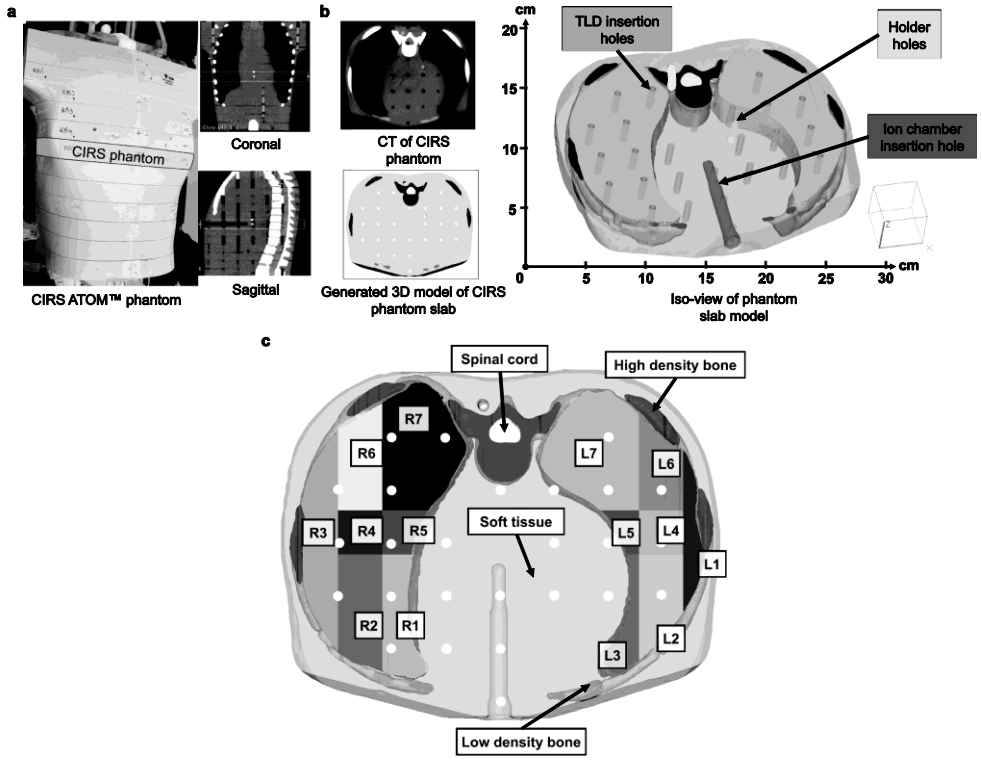

Figure 3: Generated phantom slab 3D model with a patient-specific lung lesion. (a) 3D model of the assembled phantom slab model utilizing the proposed 3D printing techniques, (b) a small spiculated lesion (squamous cell carcinoma, 5825 mm^3) with cavity (491 mm^3), positioned within the left gyroid lung sub-section, L7.

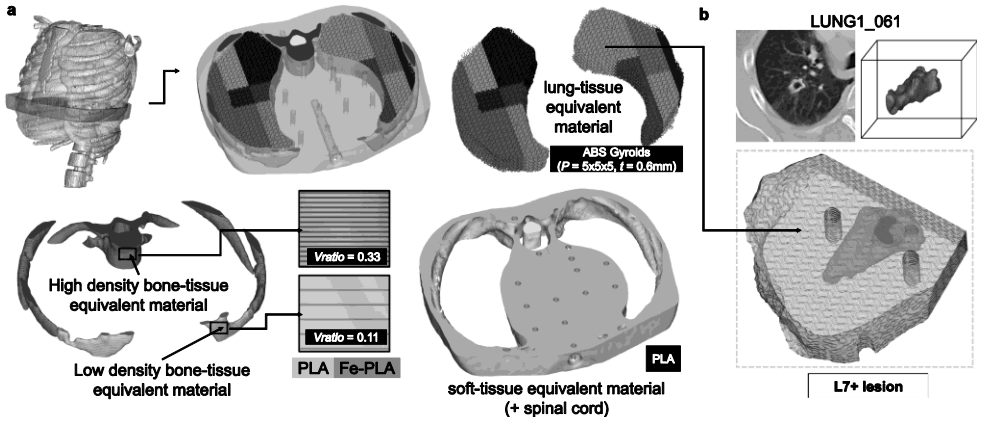

Figure 4). Two VMAT plans were generated with the 3D printed phantom for a single fraction SABR scenario. This includes a lung SABR delivering 28 Gy to the left lung gyroid sub-section L7, containing the small spiculated lesion with cavity) and a spine SABR delivering 20 Gy to T7 vertebra within the phantom. CT-simulation was performed using Philips Brilliance Big Bore with 140 kVp and 2 mm slice thickness and spacing. Three CT datasets were obtained including (1) the commercial CIRS phantom slab, (2) the 3D printed phantom slab without lesion, and (3) with lesion.

Eclipse v15.6 and TrueBeam™ STx linear accelerator with HD-MLC (Varian Medical System, Palo Alto, CA, USA) were used for all treatment planning and delivery processes. This included the use of high-resolution structure for target and adjacent organs at risk (OAR), 3-5 mm planning target volume (PTV) margin, Photon Optimizer v15.1 with structure resolution 1.25 mm, Acuros dose calculation algorithm (AXB, v15.6) with dose grid 1.25mm, and flattening filter free (FFF) beams, 6-megavoltage (MV) FFF with two 200-degree arcs and 10-MV FFF with two full 360-degree arcs for lung and spine SABR plans, respectively. Image Guided Radiation Therapy (IGRT) was performed using On-Board imager cone beam CT and ExacTrac X-ray for 6 degree-of-freedom robotic couch correction prior to beam delivery.

Dosimetric verification was performed using EBT3 radiochromic film – four sheets of film were placed inside both lung and spine PTVs (see Figure 1: Design and printing workflow of an anthropomorphic phantom. 1.) generation of phantom slab 3D model, 2.) virtual post-processing of the phantom slab 3D model, 3.) application of the proposed MEX 3D printing techniques to emulate lung-, soft-, and bone-tissue densities, 4.) slicing of the phantom slab 3D model and 5.) gyroid lung sub-sections using IdeaMaker software, 6.) printing of the phantom slab and gyroid lung sub-section 3D models.

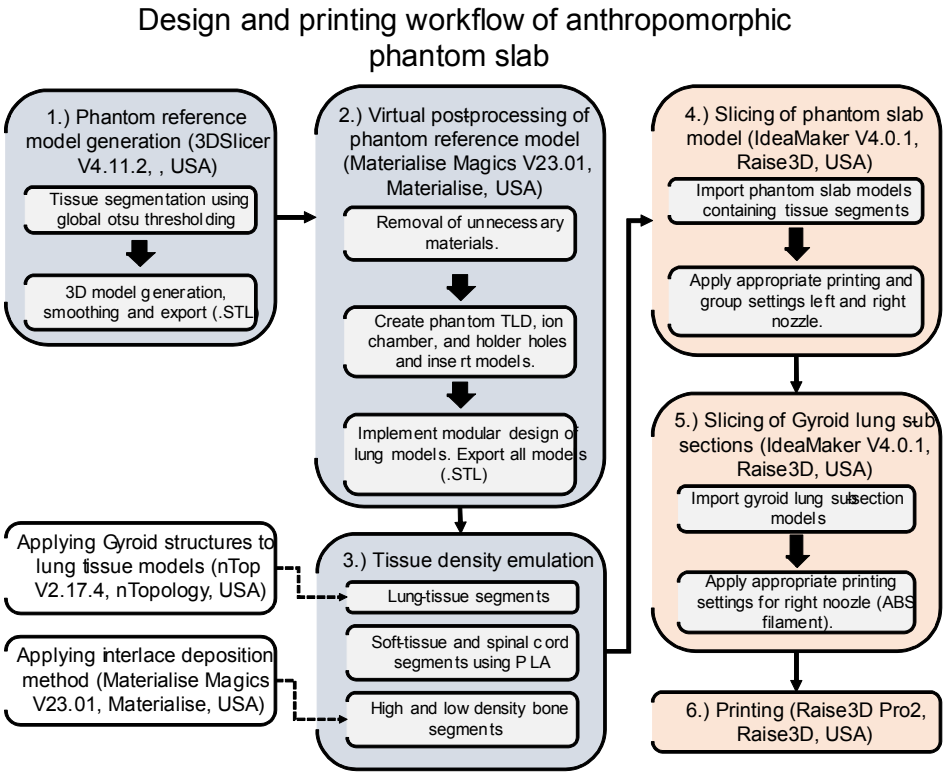

Figure 2: Segmentation and generation process of the adult CIRS ATOM phantom slab from CT for 3D printing. (a) CT of CIRS ATOM® adult phantom, (b) generated 3D phantom model with dosimetry insertion holes including holder holes for stability, TLD holders, and an ion chamber hole, (c) tissue segments including a spinal cord, high- and low- density bone, soft tissue, and lung tissue sub-sections (L1-L7 and R1-R7).

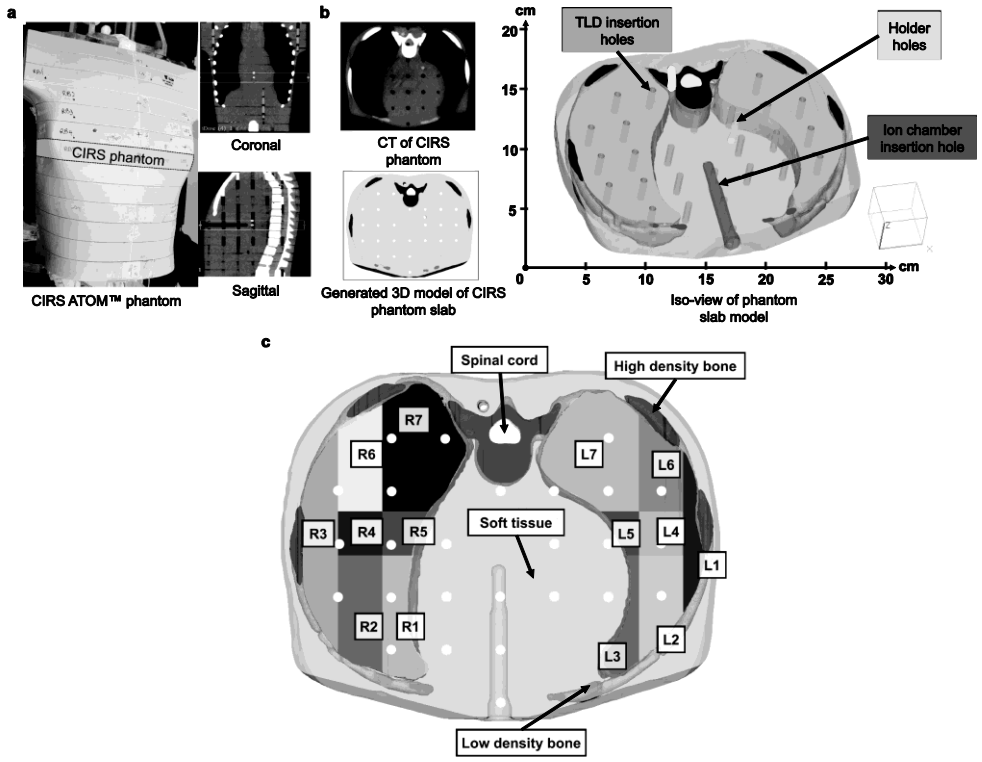

Figure 3: Generated phantom slab 3D model with a patient-specific lung lesion. (a) 3D model of the assembled phantom slab model utilizing the proposed 3D printing techniques, (b) a small spiculated lesion (squamous cell carcinoma, 5825 mm^3) with cavity (491 mm^3), positioned within the left gyroid lung sub-section, L7.

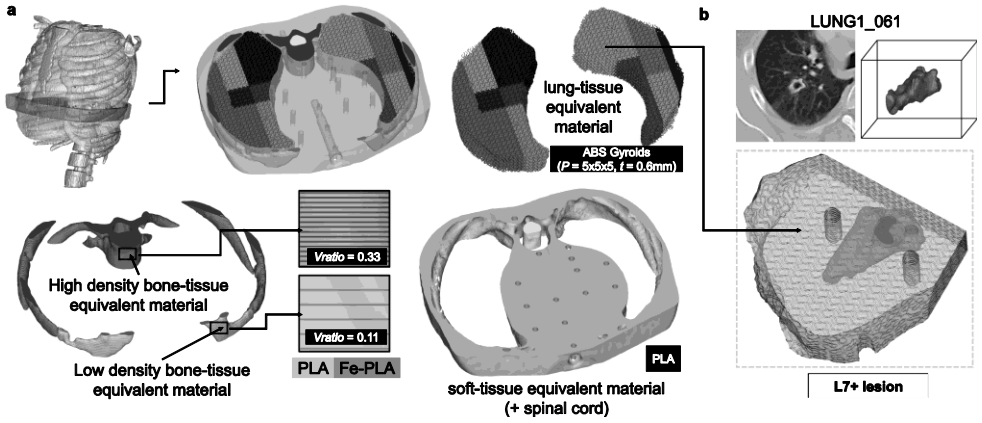

Figure 4: End-to-end testing workflow for the 3D printed anthropomorphic phantom. 1) simulation process of the 3D printed phantom using fan beam CT, 2) treatment planning process of the 3D printed phantom using Eclipse V15.6, 3) plan delivery using TrueBeam ST linear accelerator with high-definition multileaf collimator (HD-MLC), 4) and radiochromic film analysis.

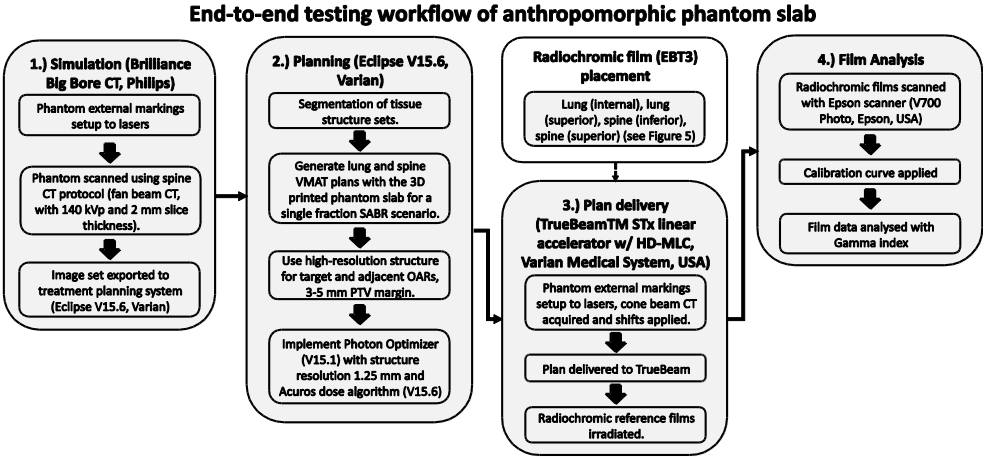

Figure 5). This set of measurements consisted of a custom cut film placed in between the sub-section L7 containing the lung lesion, a rectangular film placed superior to the sub-section L7 adjacent to the lung lesion (still inside the lung PTV). Two rectangular films were placed superior and inferior to the spinal region of the 3D printed phantom for spine SABR covering the whole spinal region including the spinal cord and some areas of the soft-tissue, and lung-tissue segments. The measured films were scanned 18 hours after irradiation using a calibrated EPSON flatbed scanner (V700 Photo, EPSON, USA). Film calibration and analysis were performed using 2D Dosimetry QA software (SNC Patient™, Sun Nuclear, USA). 2D-gamma analysis was based on absolute film dosimetry with global criteria including a dose difference (DD) of 5% and a distance to agreement (DTA) of 1 mm, with 10% low-dose threshold, according to our department clinical protocol for single fraction SABR delivery verification.

3 Results

The 3D printed phantom (excluding the gyroid lung sub-sections) resulted in a total print time of ≈61 hours (≈41 g of Fe-PLA and 792 g of PLA filament), and an estimated material and 3D printing cost of ≈37 USD. A total of fourteen gyroid lung sub-sections were manufactured separately, resulting in a total print time of ≈40 hours (≈147 g of ABS filament). The gyroid lung sub-section containing the NSCLC lesion was manufactured with a total print time of ≈7 hours (≈30 g of ABS filament) (see Figure 1: Design and printing workflow of an anthropomorphic phantom. 1.) generation of phantom slab 3D model, 2.) virtual post-processing of the phantom slab 3D model, 3.) application of the proposed MEX 3D printing techniques to emulate lung-, soft-, and bone-tissue densities, 4.) slicing of the phantom slab 3D model and 5.) gyroid lung sub-sections using IdeaMaker software, 6.) printing of the phantom slab and gyroid lung sub-section 3D models.

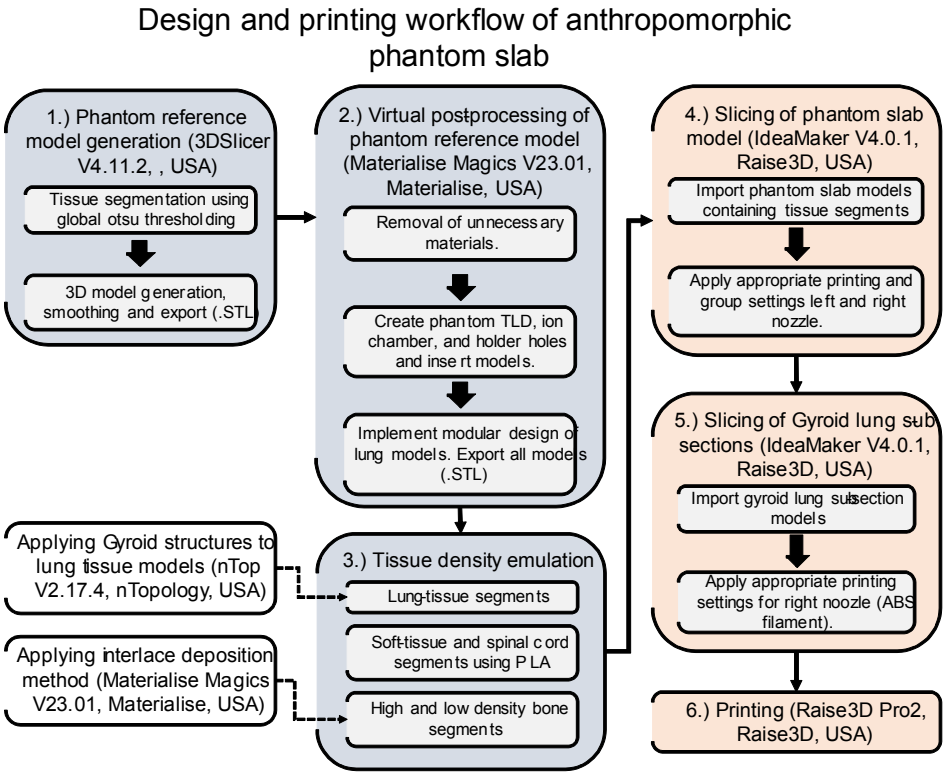

Figure 2: Segmentation and generation process of the adult CIRS ATOM phantom slab from CT for 3D printing. (a) CT of CIRS ATOM® adult phantom, (b) generated 3D phantom model with dosimetry insertion holes including holder holes for stability, TLD holders, and an ion chamber hole, (c) tissue segments including a spinal cord, high- and low- density bone, soft tissue, and lung tissue sub-sections (L1-L7 and R1-R7).

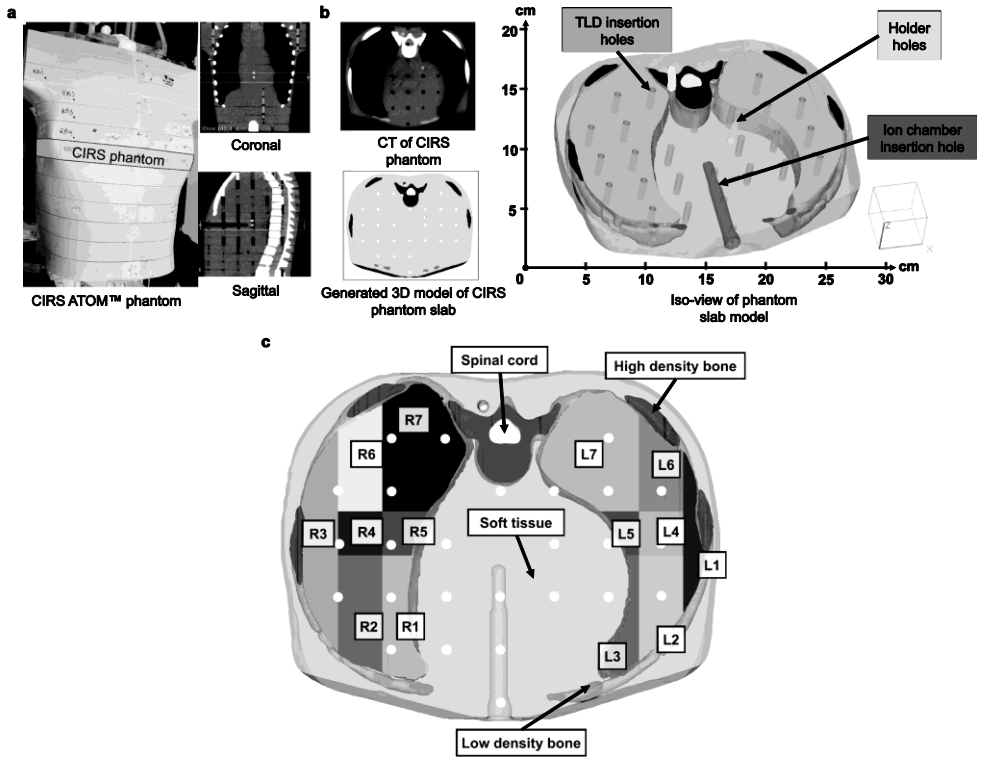

Figure 3: Generated phantom slab 3D model with a patient-specific lung lesion. (a) 3D model of the assembled phantom slab model utilizing the proposed 3D printing techniques, (b) a small spiculated lesion (squamous cell carcinoma, 5825 mm^3) with cavity (491 mm^3), positioned within the left gyroid lung sub-section, L7.

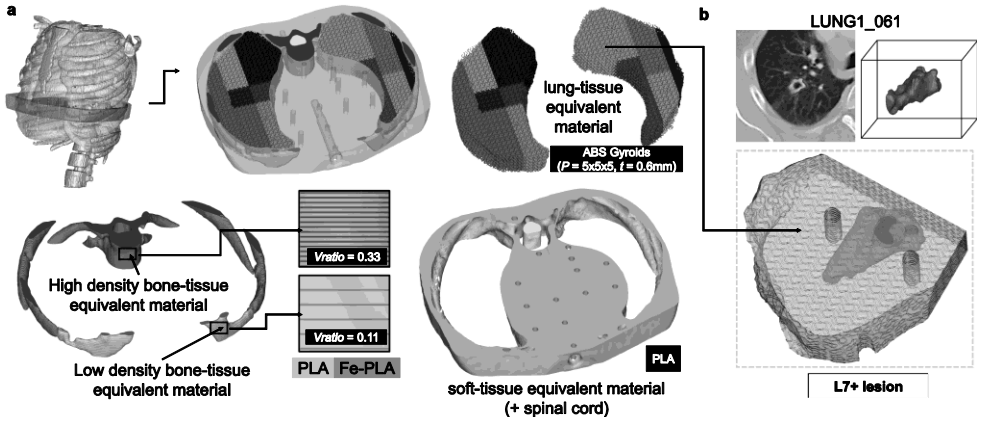

Figure 4: End-to-end testing workflow for the 3D printed anthropomorphic phantom. 1) simulation process of the 3D printed phantom using fan beam CT, 2) treatment planning process of the 3D printed phantom using Eclipse V15.6, 3) plan delivery using TrueBeam ST linear accelerator with high-definition multileaf collimator (HD-MLC), 4) and radiochromic film analysis.

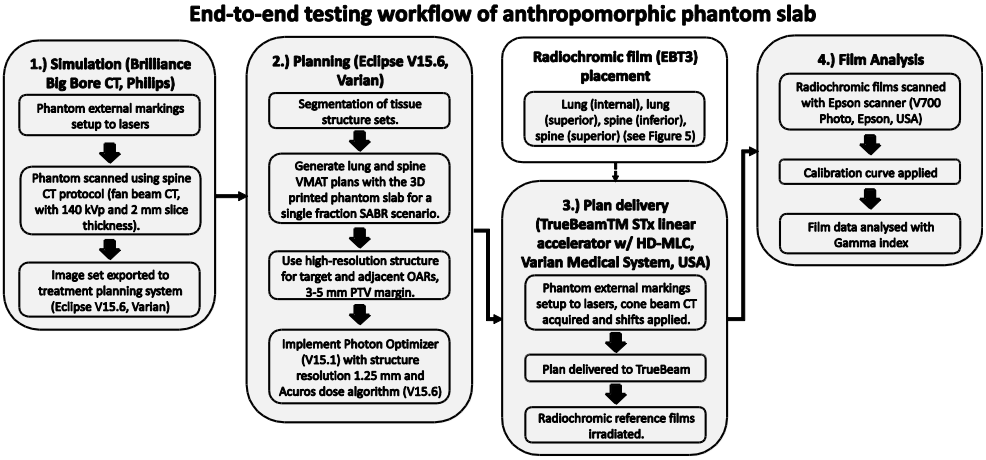

Figure 5).

3.1 Imaging verification

From CT imaging results of the ED phantom, the gyroid parameter with a *P* of 5 and a *t* of 0.6 mm was observed to produce lung-equivalent density, with a mean HU of -755±8 at 140 kVp. For fabricating a lung lesion density material, an additional ED insert was manufactured using the same ABS material at 100% infilling, which were observed to produce a mean HU of -119±18 at 140 kVp, which is an acceptable range for lung lesion densities found in various lung cancer patients (See complete results of printed gyroid phantom inserts in Appendix A). Other 3D printed phantom inserts including the interlace deposition phantom inserts using PLA and Fe-PLA filaments were found consistent with results from the authors' previous study[22]. The CT results in **Error! Reference source not found.** were utilized to validate the intended materials and structures to be used for designing and manufacturing the phantom slab.

Further quantitative evaluation of the 3D printed gyroid lung sub-section, L7 at 140 kVp, by comparing contour data, were observed with a mean HU of -244 ± 150 (lesion) and -765 ± 33 (lung) for sample 1, a mean HU of -261 ± 171 (lesion) and -765 ± 43 (lung) for sample 2, and a mean HU of -245 ± 160 (lesion) and -764 ± 50 (lung) for sample 3 (see Appendix B).

3.2 End-to-end testing

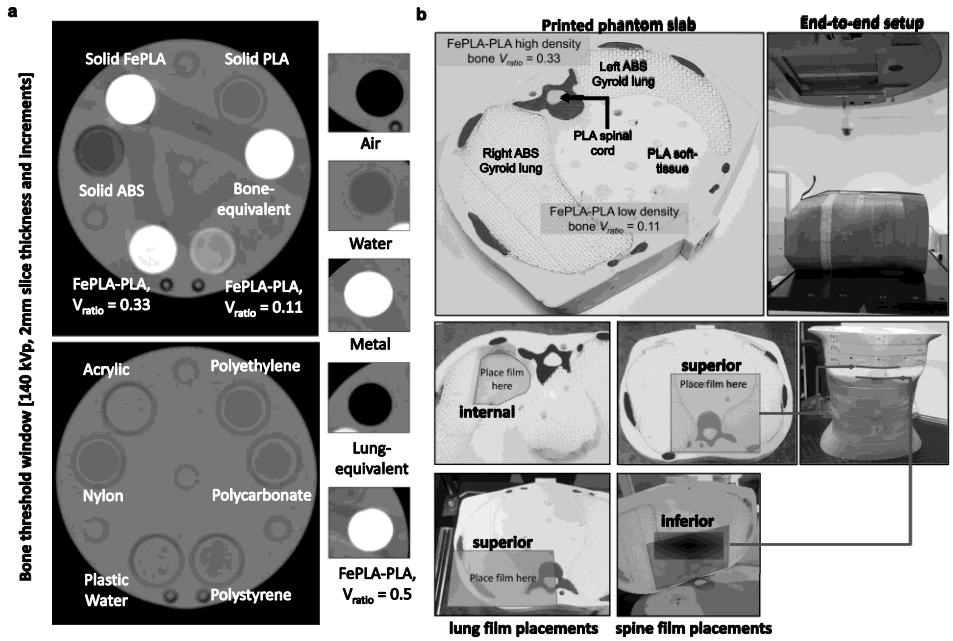

*Figure 6*a below illustrates the initial CT imaging process for the end-to-end testing. Compared to the commercial CIRS phantom, the 3D printed phantom was observed to have a very similar CT attenuation (in HU) as shown by the generated line profiles in

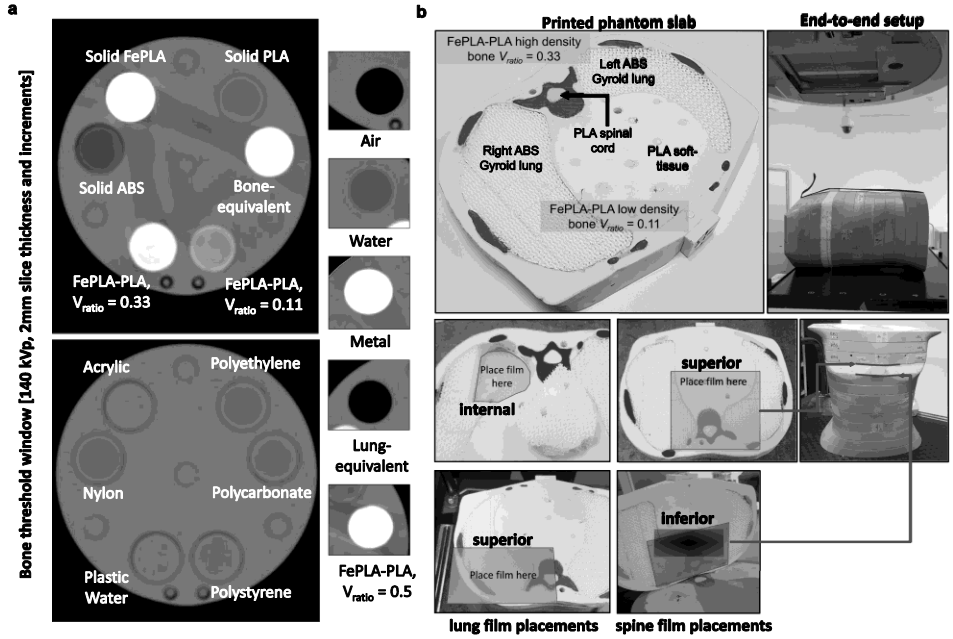

*Figure 6*b-c. Minor discrepancies in HU were observed between the CIRS phantom and the 3D printed phantom, which mainly consists of differences due to printed ion chamber insert and the subtle effects of beam hardening artefacts due to the presence of iron particle content in the bone regions. **Error! Reference source not found.** shows the extracted mean HU and standard deviations comparing the CIRS phantom, the 3D printed phantom, and the lesion, utilising the generated tissue contours.

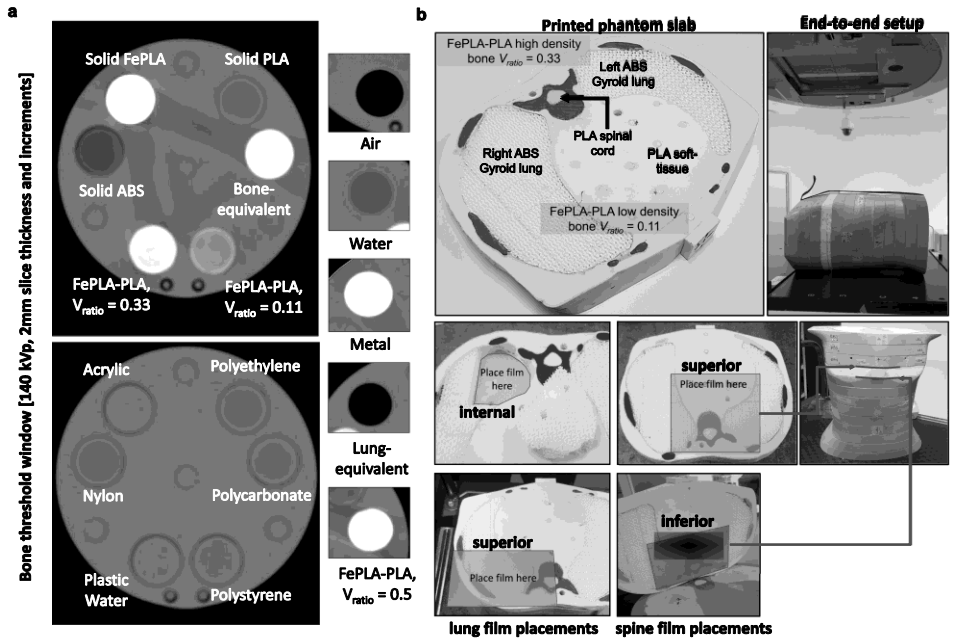

Figure 6: CT comparison of commercial CIRS Phantom and 3D printed phantom slabs. (a) alignment and scanning of phantoms, (b) drawn line profiles for CIRS phantom and the 3D printed phantom, (c) line profiles 1-5 comparing the HU of CIRS phantom and the 3D printed phantom: i, HU difference due to a missing ion chamber insert in the commercial CIRS phantom, ii, presence of high-density shells in the 3D printed phantom, iv, the limited resolution of the CT produced a slightly inaccurate representation of the 3D printed model.

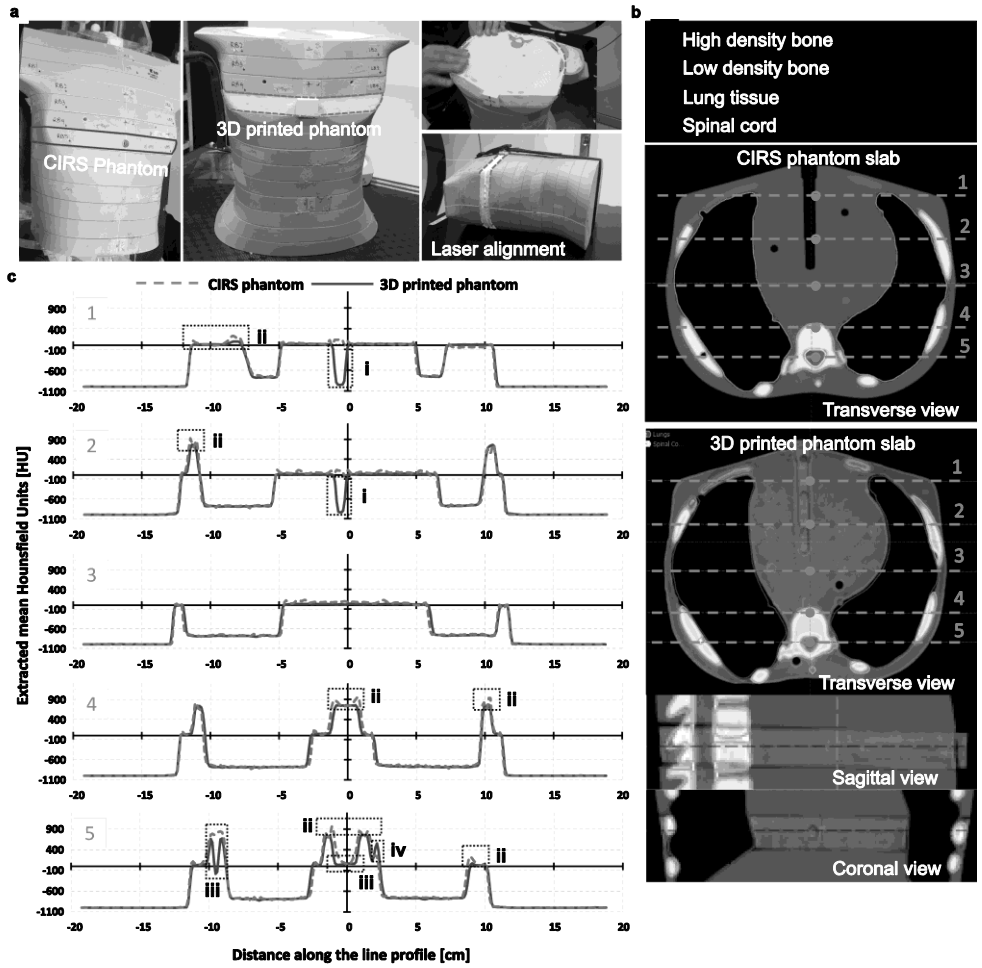

Figure 7 shows dosimetric verification results for both lung and spine SABR cases at measured film planes, a: plan dose overlaid to CT image, b: film scan, c: measured dose, and d: 2D gamma map. Global gamma criteria of 5% DD and 1 mm DTA resulted in gamma passing rates for the lung (internal/superior) and the spine films (inferior/superior) of 99.8 %/98.0% and 90.2%/90.3%, respectively. Both cases show clinically acceptable agreement in various tissue types, including lung-, bone- and soft-tissues. Line profile analysis in

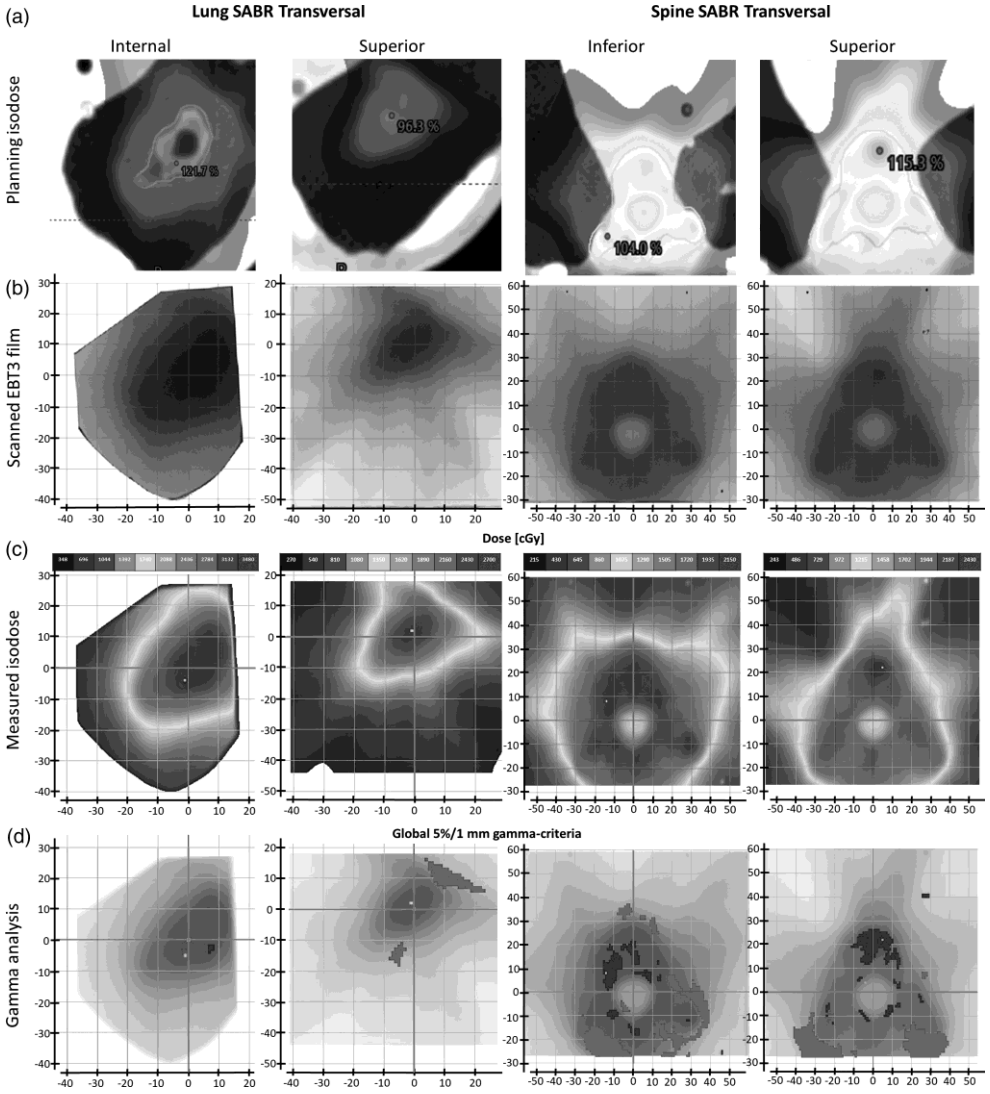

Figure 8 shows similarities at the interface of different tissue types (e.g., lung to soft-tissue, bone to soft-tissue and lung to bone), including dose-drop off at spinal cord, which indicates tissue-equivalence of the 3D printed phantom for MV-photon modelling.

4 Discussion

This work demonstrated the design and development of a customized anthropomorphic phantom, the 3D printed phantom, which utilizes inexpensive MEX 3D printing material filaments and techniques. CT imaging results show that the 3D printed phantom produced heterogeneous densities that accurately emulate bone-, soft-, and lung-tissue HU. Furthermore, the 3D printed phantom demonstrated clinical feasibility for the end-to-end testing of complex SABR treatment scenarios in the spine and lung with a cavitating lesion, making it suitable for MV-photon modelling. Further investigation of this work may have the potential for developing clinically functional anthropomorphic phantoms for imaging and end-to-end testing applications, warranting that the appropriate equipment, printing settings, and techniques are used.

Until recently, the limited knowledge in low-cost MEX printing technology and its capabilities to emulate different tissue densities has restricted the research focus on anthropomorphic phantoms only for lung[14, 15, 19, 24], liver[25], and head & neck applications.[8] Currently, the literature in MEX printing materials and techniques has significantly grown. Researchers are now given a range of options to select different materials with varying radiological properties to emulate a wide range of soft-tissue, lung -tissue, and bone-tissue densities. Here, we demonstrate the capability of low-cost MEX 3D printing technology, leveraging existing techniques already published in the literature.[21, 22, 26] CT Imaging verification results from the 3D printed phantom inserts were shown to produce the required HU and electron density values, comparable to the commercial phantom inserts shown in **Error! Reference source not found.**. Preliminary work show that the 3D printed ABS gyroid insert produced a mean HU of -755 ± 8 similar to the commercial lung-equivalent insert with a mean HU of -797 ± 25, suggesting that ABS gyroid structures are a good candidate for emulating lung-tissue density for kV imaging domain.[21] Similarities were also observed between the PLA solid insert with a mean HU of 84 ± 15 and the commercial plastic water insert with mean HU of 100 ± 3, demonstrating its suitability for emulating soft-tissue densities, and agrees with existing literature.[22, 27-29] The various interlace deposition inserts with V_{ratio} values of 0.11, 0.33, and 0.50 produced a mean HU ranging from 280 to 1100 HU, which further suggests that the interlace deposition method provides good approximation of bone-like densities.[22]

After further analysis of CT imaging verification results, the following materials and methods were determined to design the 3D printed phantom: PLA filament printed in solid at 100% infill for the spinal cord and soft-tissue segments; ABS filament printed with gyroid structure (P =5×5×5 mm^3 and t = 0.6 mm) at 100% infill for the lung-tissue segment and the same material printed in solid at 100% infill for the lung lesion segment; the dual-extrusion of PLA and Fe-PLA filaments using the interlace deposition method to print the high-density and low-density bone segments. PLA material was selected to emulate the soft-tissue segment. It is already well established in the literature by numerous studies regarding PLA and their capabilities to

produce a good approximation of soft-tissue densities.[27, 28, 30-34] This also applies to ABS material shown by various studies to emulate lung-tissue densities by controlling its infill percentage with grid structures to vary its volume density.[29, 34, 35] However, previous work[21] have shown that standard infill grid structures produce inconsistent HU values when scanned at different specimen orientations. Here, controlling the periodicity and wall thickness of gyroid structures can accurately emulate lung-tissue densities and its isotropicity in CT imaging, thus provide sufficient approximation of lung-tissue densities for radiotherapy applications. Appendix A shows a more detailed result of 3D printed ABS gyroid phantom inserts with a full factorial design of periodicity and wall thickness parameters, assessed using different kV-CT energies. More recently, the interlace deposition method[22] which utilizes dual-extrusion printing of Fe-PLA and PLA filament, exploiting their material layer thickness ratio, V_{ratio}, were shown to achieve the full range of adult bone densities including cancellous, cortical and red bone marrow. We found that a V_{ratio} of 0.33 produced a mean HU of 631 ± 241 from the 3D printed phantom slab, which closely emulates the reference HU value for high-density bone with known mean HU of 723 ± 48. Despite this, the interlace deposition method was unable to emulate the known reference mean HU of 85 ± 22 for low-density bone. Here, the method was only able to produce a V_{ratio} of 0.11 with a mean HU of 218 ± 97, which is in agreement with the limitation stated in the study due to high iron content and surrounding shells.[22] This limitation can be addressed by using only PLA filament for the low-density bone segment in the future, however, it is to be expected that imaging contrast between the soft-tissue and the low-density bone will reduce due to the use of identical PLA material.

The thoracic phantom slab was manufactured with a total print time of ≈100 hours (980g worth of materials) with an estimated material and 3D printing cost of ≈150 USD using a dual-extrusion printer. Contours were initially generated from the CT data of the commercial CIRS phantom shown in

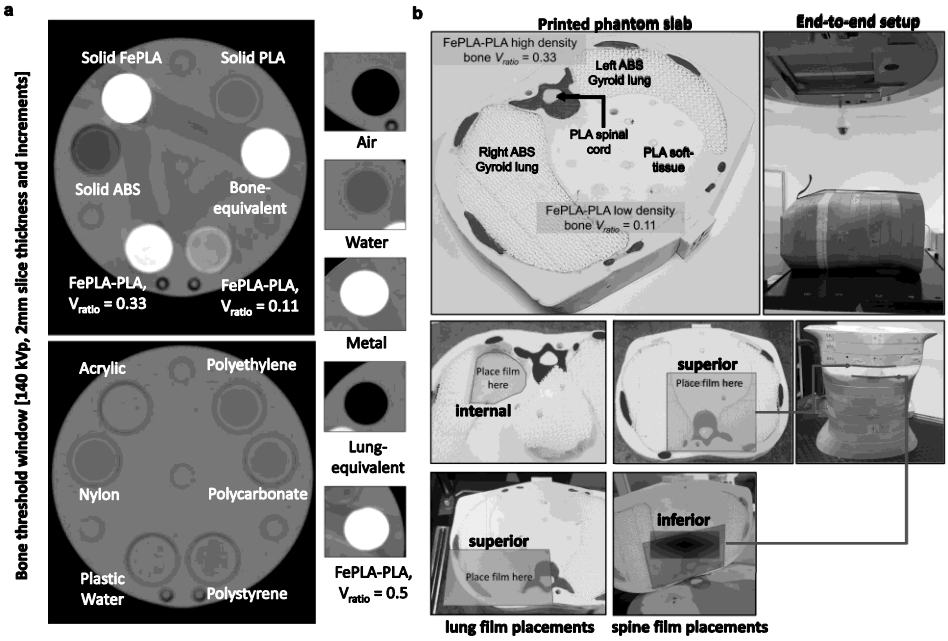

Figure 6a-b and were utilized to extract mean HU and SD values shown in **Error! Reference source not found.** from the 3D printed phantom. Mean HU results were observed to be in good agreement with the expected HU values from previous studies.[21, 22] Figure 6c show similar attenuations between the 3D printed phantom and the commercial CIRS phantom through the generated line profiles comparing the HU attenuation across both phantoms. However, there exist noticeable differences, including the presence of the ion chamber inserts and the missing region in the 3D printed phantom due to the limited resolution of the CT, producing a slightly inaccurate representation of the 3D model prior to printing (

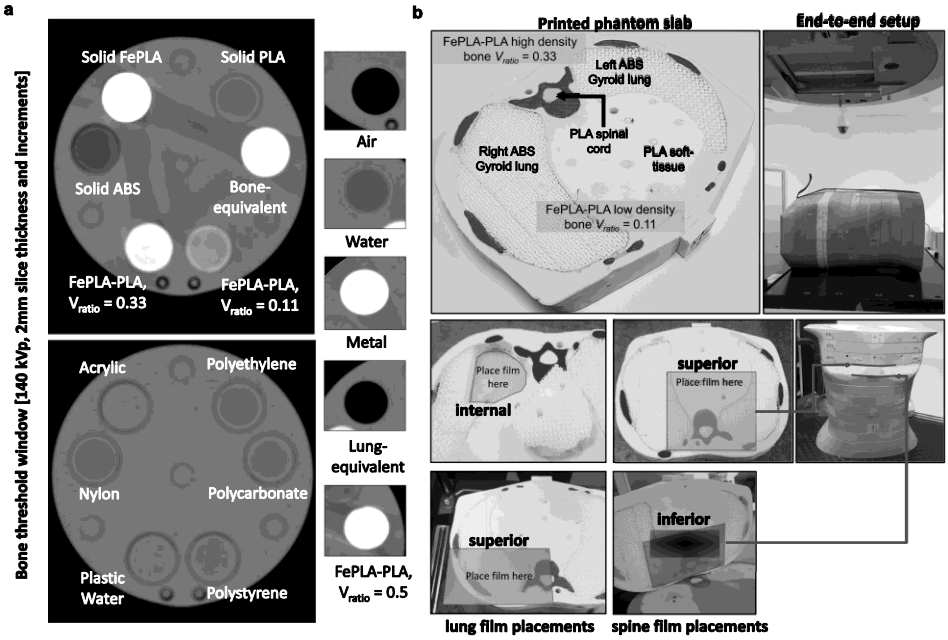

Figure 6c, i, iv) and beam hardening artefacts due to the iron content of the Fe-PLA filament (

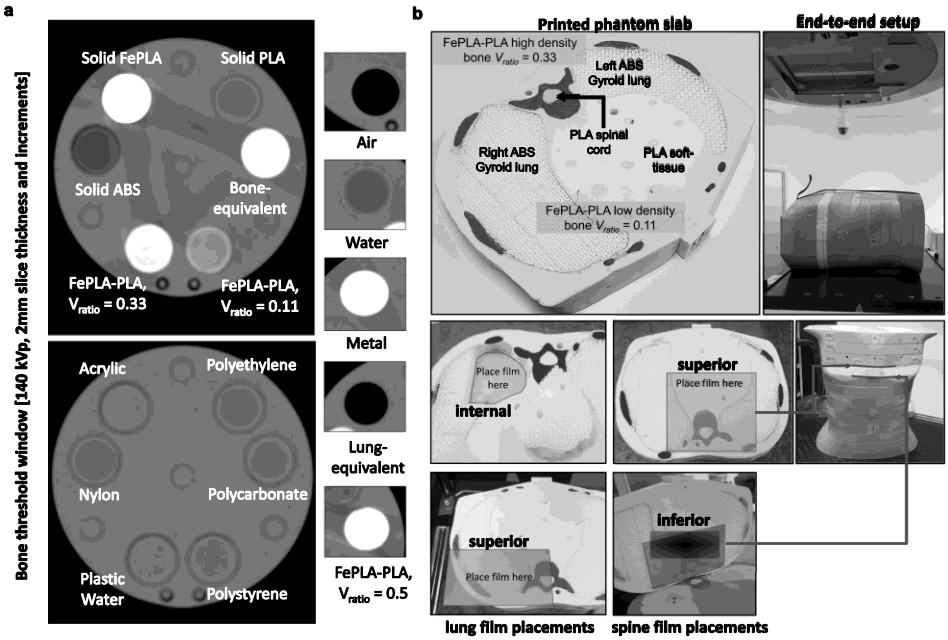

Figure 6c, ii, iii). For the printed gyroid lung structures, difficulties in characterizing variations arise due to the limited resolution of CT; therefore, they can potentially hide inaccuracies within the structures which may affect CT results. As shown in Appendix B, further evaluation of the manufactured gyroid lung samples using conventional fan beam CT, was observed with slight discrepancies in the lung tissue sections within acceptable ranges, whereas the lesion section produced identical attenuations.

Lung and spine SABR plans were generated according to our department's clinical protocol as part of the end-to-end testing to experimentally validate the clinical usability of our customized anthropomorphic phantom for a range of heterogeneity scenarios including the presence of a cavitating lesion (see

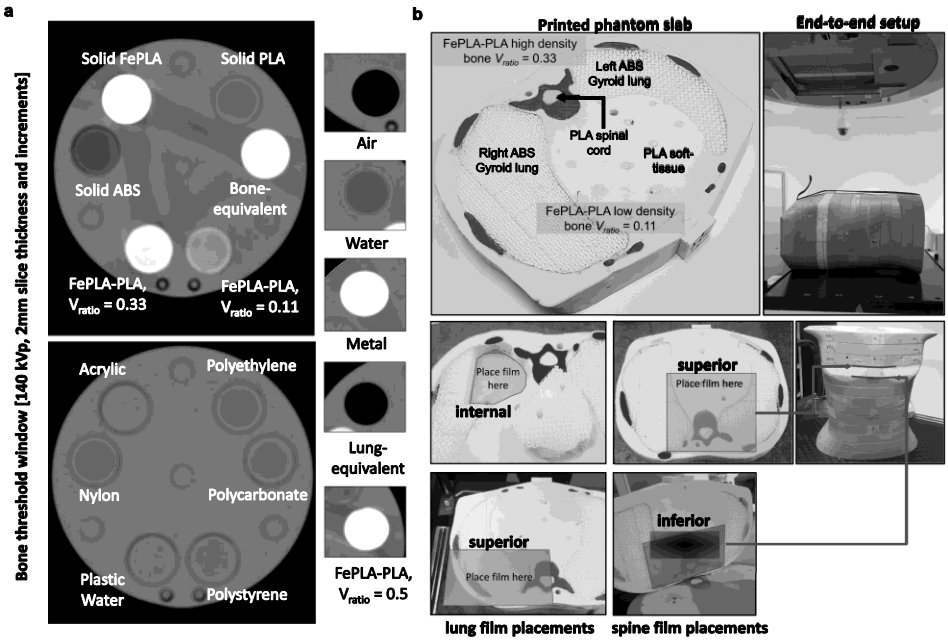

Figure 6: CT comparison of commercial CIRS Phantom and 3D printed phantom slabs. (a) alignment and scanning of phantoms, (b) drawn line profiles for CIRS phantom and the 3D printed phantom, (c) line profiles 1-5 comparing the HU of CIRS phantom and the 3D printed phantom: i, HU difference due to a missing ion chamber insert in the commercial CIRS phantom, ii, presence of high-density shells in the 3D printed phantom, iv, the limited resolution of the CT produced a slightly inaccurate representation of the 3D printed model.

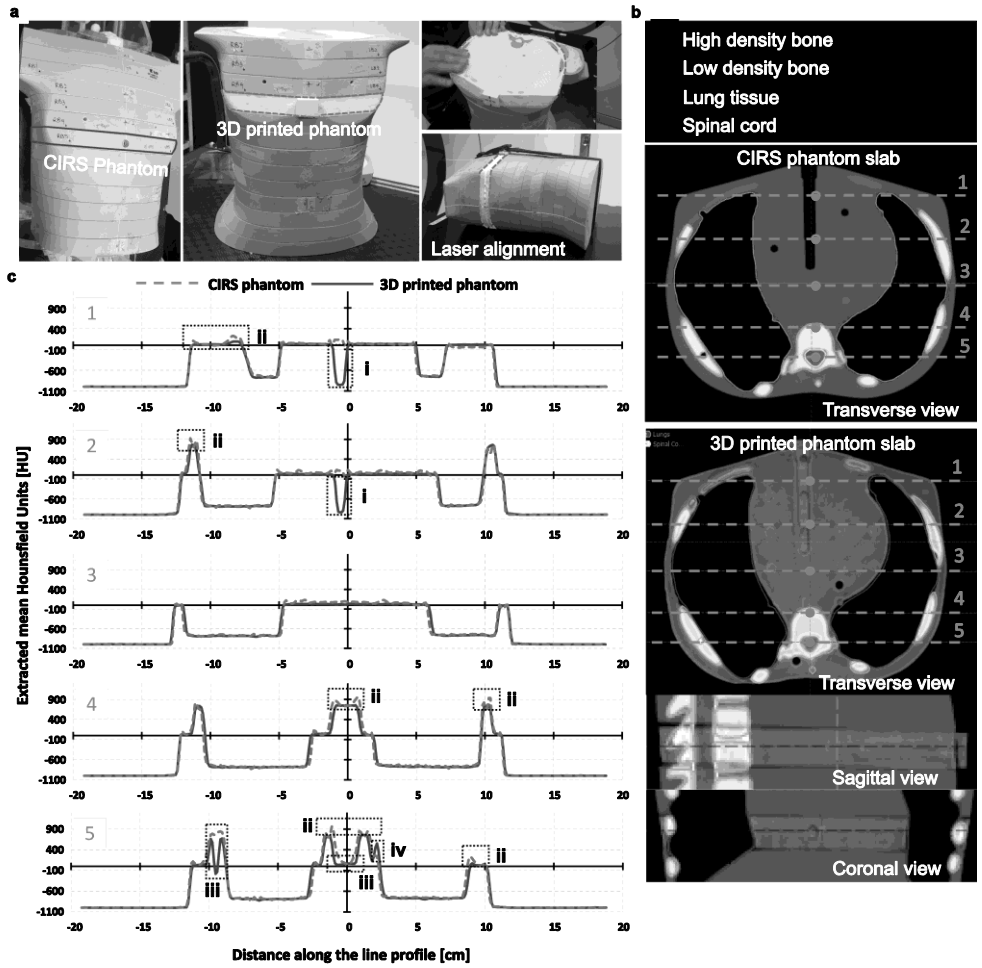

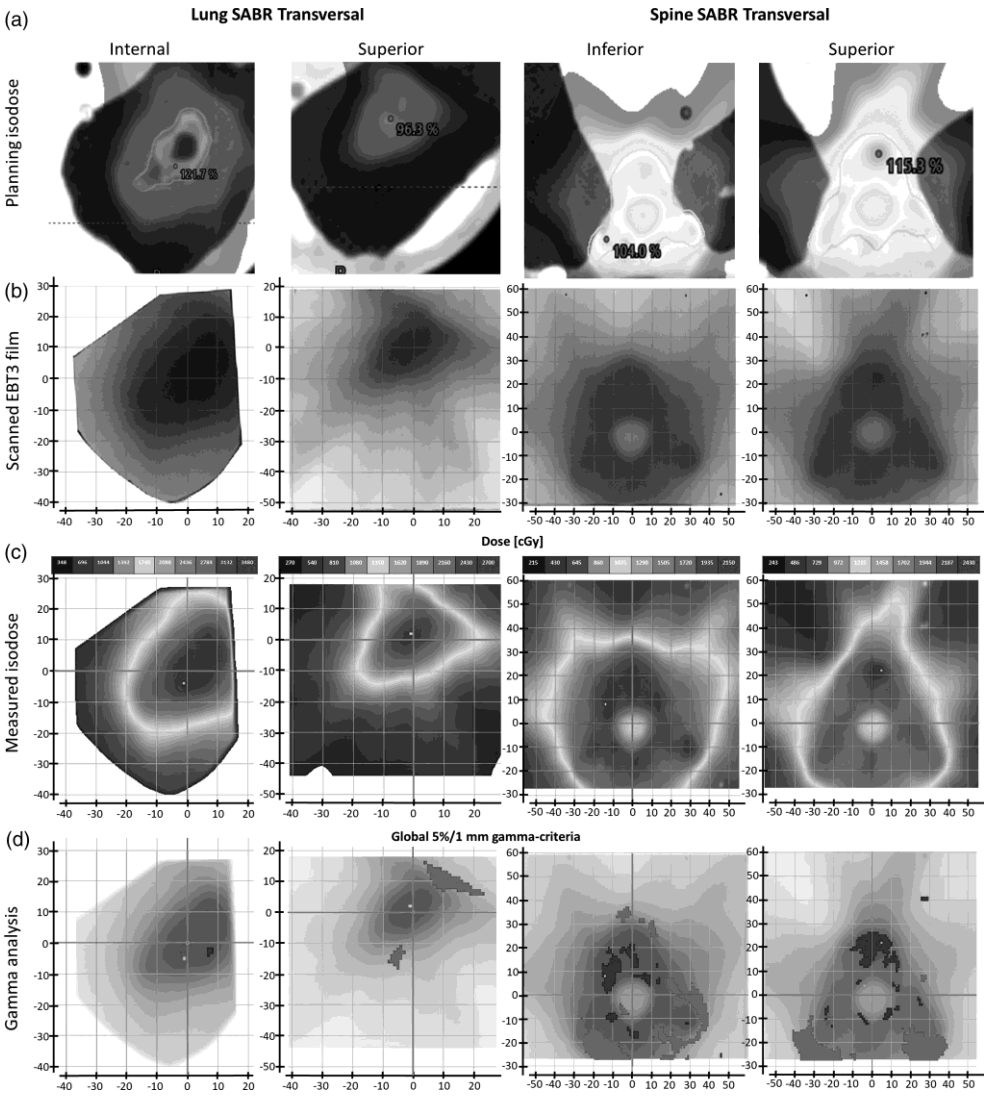

Figure 7 and

Figure 8). It is important to note that only a single fraction SABR dose regime was used including a 28 Gy per fraction for lung and 20 Gy per fraction for T7 spine, to verify tissue densities for megavoltage photon beams at the interface of different tissue types (bone-soft tissue, soft tissue-lung and lung-bone). EBT3 film measurements show clinically acceptable agreements in various tissue types for lung, soft-tissue, and bone. According to our departmental SABR protocol for hypofractionated dose regimes, using 5% DD and 1 mm DTA was deemed appropriate for this scenario, in addition to being a suitable gamma criteria for 2D gamma analysis in SABR level three dosimetry audits.

Despite good imaging and dosimetry results of the 3D printed phantom, limitations were observed across the development and end-to-end testing process of the phantom and should be given careful consideration for the future development of this technology in radiotherapy. Design limitations include: the modular design of the gyroid lung sub-sections, which inherently produces slightly noticeable gaps in CT between sub-sections due to the clearance used to allow easier part assembly; the absence of film fixations across the 3D printed phantom, when not correctly adhered on the phantom, the film will likely be displaced, leading to inaccurate dose measurements; and since only one phantom section was designed and manufactured, measurement limitations of the 3D printed phantom exist which limits the allowable size of a lesion that can be examined. Manufacturing limitations include: the extrusion of unnecessary materials during printing when using the dual-extrusion of Fe-PLA and PLA[22]; and the rough surfaces produced when printing overhanging features, preventing the use of ion chamber for dose measurements and should require further post-processing to correct surface imperfections and allow non-obstructive insertion of ion chambers. The variabilities in the quality of 3D printed phantoms using material extrusion technology arise from different factors such as filament material composition and density, material printing parameters (i.e., layer height, speed, temperature), and machine specifications, of which these factors may further vary between different manufacturers.[36] Another factor which is yet to be fully characterized in the imaging and dosimetry domain for radiotherapy applications is the color pigments utilized in commercial 3D printing filaments. For PLA filaments, it has been found that different colors lead to different degradation and glass temperatures, which were shown to affect surface quality under the same printing parameters[37] and was further shown to also affect tensile properties[38] and crystallinity.[39] This suggests that color may potentially have direct effects towards the physical properties of 3D printing filaments, thus influencing the kV imaging and MV photon attenuations of 3D printed parts.

Moving towards clinical translation, robust uncertainty quantification programs for 3D printed phantoms—to address epistemic uncertainties due to the lack of knowledge of a parameter or process and aleatory uncertainties which are derived from intrinsic randomness—must be a critical consideration when certifying their use for high-value applications such as routine personalized treatment planning and QA of new treatment machines. High resolution micro-CT imaging techniques can likely be used to reduce epistemic uncertainties produced by the 3D printing process (i.e., manufacturing limitations such as the presence of internal pores, shape discrepancies, and low surface quality) and improve process parameters to address manufacturing limitations and minimise resulting imaging and dosimetry variabilities. Furthermore, relevant

machine calibration processes, printing parameters, and the use of different 3D printers and filament manufacturers must be implemented and adequately documented for reproducibility. Aleatory uncertainties include the stochastic nature of HU within a region of interest of a material—understanding deviations of HU within a given 3D printing material will provide researchers with a tool for optimal material selection processes. Thus, addressing these uncertainties will enable systematic certification programs in manufacturing 3D printed phantoms to avoid manufacturability and reproducibility issues.

The 3D printing's capabilities for reduced costs, faster manufacturing lead-times, and free-form fabrication is seen as a great research opportunity in the medical field. Tissue-equivalence of the 3D printed phantom in this work was only examined for kilovoltage and megavoltage photon beams, thus it is only tissue-equivalent to a limited extent. Although comparable to the commercial CIRS phantom in megavoltage photon beam scenarios, tissue-equivalence of the 3D printed phantom in electron and proton scenarios are yet to be verified, in addition to sealed source brachytherapy and unsealed source for nuclear medicine. Such limitations highlighted above finds great venue of future research for the generative design of the 3D printed phantom and the uncertainty quantification of the phantom manufacturing process, for further cost reduction and enhanced personalization, sustainability, and functionality. There is a crucial need in routine clinical settings to require custom-made phantoms because available commercial phantoms are mostly expensive and are simplified forms of patient anatomy, thus cannot be modified easily. With the proposed 3D printing techniques, different sizes of features can be added with different densities to test different imaging protocols systematically. Complex radiotherapy scenarios can be also emulated for validation purposes, which will be beneficial to design comprehensive imaging and dosimetry audits such as the emulation of metal implants in phantoms.[40] More complex lung scenarios are to be investigated to systematically study behaviors of different deformable image registration algorithms, potentially beneficial for future clinical trial audits utilising similar advanced imaging tools for multi-modality target delineation and deformable dose accumulation.[15, 17, 41, 42] This application can be extended towards the 3D printing of realistic phantoms with a mixture of solid and deformable walls, filled with deformable carrageenan-based materials for the enhanced physical emulation of organ deformation.[20] Different tissue type inserts can be made within an anthropomorphic setting to validate dual-energy CT contrast resolution of the various tissue types, which is important for particle therapy dose calculation modelling as mapping the stopping power ratio for different tissue types is one of the key sources in beam range uncertainty. Other advanced applications also include molecular imaging[43], ultrasound cardiac applications[44], adaptive radiotherapy for MR-guided system[45], and radiomics-based texture metrics.[46]

5 Conclusions

In this study, we demonstrated the use of material extrusion 3D printing to develop a customizable anthropomorphic phantom slab consisting of different tissue density materials for lung, soft-tissue, and bone. Tissue-equivalent densities of the 3D printed phantom was evaluated through kV-CT imaging, which produced similar HU attenuations observed from the commercial phantom. The end-to-end testing using

SABR clinical protocol further validate the clinical feasibility of the 3D printed phantom slab for MV photon dosimetry. A better understanding of uncertainties from 3D printed phantoms will enable clinical potential across other applications, including proton therapy quality assurance, deformable image registration, adaptive dosimetry, nuclear medicine, and radiomics.

Acknowledgements

This research was supported by the Australian Research Council (ARC) Industrial transformation Training Centre in Additive Biomanufacturing (IC160100026). http:// www.additivebiomanufacturing.org and the Gross Foundation. Authors acknowledge the use of facilities within the RMIT Advanced Manufacturing Precinct and nTopology for the academic license. We would also like to acknowledge Sir Peter MacCallum Cancer's Physical Sciences department for allowing us to use their CT and LINAC machines and the Biomedical Engineering department for allowing us to use their 3D printer.

Conflict of Interest Statement

The authors have no relevant conflicts of interest to disclose.

Data Availability

CT datasets and .STL models (phantom inserts and phantom slab) are available by request from Tomas.Kron@petermac.org.

References

1. Mutic S, Palta JR, Butker EK, et al. Quality assurance for computed-tomography simulators and the computed-tomography-simulation process: Report of the AAPM Radiation Therapy Committee Task Group No. 66. *Medical Physics*. 2003;30(10):2762-2792. doi:https://doi.org/10.1118/1.1609271

2. Kutcher GJ, Coia L, Gillin M, et al. Comprehensive QA for radiation oncology: Report of AAPM Radiation Therapy Committee Task Group 40. *Medical Physics*. 1994;21(4):581-618. doi:https://doi.org/10.1118/1.597316

3. Lehmann J, Alves A, Dunn L, et al. Dosimetric end-to-end tests in a national audit of 3D conformal radiotherapy. *Physics and Imaging in Radiation Oncology*. 2018/04/01/ 2018;6:5-11. doi:https://doi.org/10.1016/j.phro.2018.03.006

4. Followill DS, Evans DR, Cherry C, et al. Design, development, and implementation of the Radiological Physics Center's pelvis and thorax anthropomorphic quality assurance phantoms. *Medical Physics*. 2007;34(6Part1):2070-2076. doi:https://doi.org/10.1118/1.2737158

5. Walter C, Boda-Heggemann J, Wertz H, et al. Phantom and in-vivo measurements of dose exposure by image-guided radiotherapy (IGRT): MV portal images vs. kV portal images vs. cone-beam CT. *Radiotherapy and Oncology*. 2007/12/01/ 2007;85(3):418-423. doi:https://doi.org/10.1016/j.radonc.2007.10.014

6. Janssens G, Orban de Xivry J, Fekkes S, et al. Evaluation of nonrigid registration models for interfraction dose accumulation in radiotherapy. *Medical Physics*. 2009;36(9Part1):4268-4276. doi:https://doi.org/10.1118/1.3194750

7. Gallo JJ, Kaufman I, Powell R, et al. Single-fraction spine SBRT end-to-end testing on TomoTherapy, Vero, TrueBeam, and CyberKnife treatment platforms using a novel anthropomorphic phantom. *Journal of Applied Clinical Medical Physics*. 2015;16(1):170-182. doi:https://doi.org/10.1120/jacmp.v16i1.5120

8. Ehler E, Barney B, Higgins P, Dusenbery K. Patient specific 3D printed phantom for IMRT quality assurance. *Physics in Medicine & Biology*. 2014;59(19):5763. doi:https://doi.org/10.1088/0031-9155/59/19/5763

9. Ehler E, Craft D, Rong Y. 3D printing technology will eventually eliminate the need of purchasing commercial phantoms for clinical medical physics QA procedures. *Journal of Applied Clinical Medical Physics*. 2018;19:8. doi:http://dx.doi.org/10.1002/acm2.12392

10. Filippou V, Tsoumpas C. Recent advances on the development of phantoms using 3D printing for imaging with CT, MRI, PET, SPECT, and ultrasound. *Medical Physics*. 2018;45:e740. doi:https://doi.org/10.1002/mp.13058

11. Tino R, Leary M, Yeo A, Kyriakou E, Kron T, Brandt M. Additive manufacturing in radiation oncology: a review of clinical practice, emerging trends and research opportunities. *International Journal of Extreme Manufacturing*. 2020;2(1):012003. doi:https://doi.org/10.1088/2631-7990/ab70af

12. Tino R, Yeo A, Leary M, Brandt M, Kron T. A systematic review on 3D-printed imaging and dosimetry phantoms in radiation therapy. *Technology in Cancer research & Treatment*. 2019;18doi:https://doi.org/10.1177/1533033819870208

13. Craft DF, Kry SF, Balter P, Salehpour M, Woodward W, Howell RM. Material matters: Analysis of density uncertainty in 3D printing and its consequences for radiation oncology. *Medical Physics*. 2018;45(4):1614-1621. doi:https://doi.org/10.1002/mp.12839

14. Yoon KJ, Kwak JW, Cho BC, et al. Development of new 4D phantom model in respiratory gated volumetric modulated arc therapy for lung SBRT. *Progress in Medical Physics*. 2014;25(2):100-109. doi:http://dx.doi.org/10.14316/pmp.2014.25.2.100

15. Jung J, Song SY, Yoon SM, et al. Verification of Accuracy of CyberKnife Tumor-tracking Radiation Therapy Using Patient-specific Lung Phantoms. *International Journal of Radiation Oncology, Biology, Physics*. 2015;92(4):745-753. doi:10.1016/j.ijrobp.2015.02.055

16. Zhang F, Zhang H, Zhao H, et al. Design and fabrication of a personalized anthropomorphic phantom using 3D printing and tissue equivalent materials. *Quantitative Imaging in Medicine and Surgery*. 2019;9:94. doi:10.21037/qims.2018.08.01

17. Yoon KJ, Jeong C, Kim S-W, et al. Dosimetric evaluation of respiratory gated volumetric modulated arc therapy for lung stereotactic body radiation therapy using 3D printing technology. *PLoS One*. 2018;13(12):e0208685-e0208685. doi:https://doi.org/10.1371/journal.pone.0208685

18. Hazelaar C, Van Eijnatten M, Dahele M, et al. Using 3D printing techniques to create an anthropomorphic thorax phantom for medical imaging purposes. *Medical Physics*. 2018;45:92. doi:https://doi.org/10.1002/mp.12644

19. Mayer R, Liacouras P, Thomas A, Kang M, Lin L, Simone CB. 3D printer generated thorax phantom with mobile tumor for radiation dosimetry. *Review of Scientific Instruments*. 2015;86:074301. doi: https://doi.org/10.1063/1.4923294

20. Singhrao K, Fu J, Wu HH, et al. A novel anthropomorphic multimodality phantom for MRI-based radiotherapy quality assurance testing. *Medical Physics*. 2020;47(4):1443-1451. doi:https://doi.org/10.1002/mp.14027

21. Tino R, Leary M, Yeo A, Brandt M, Kron T. Gyroid structures for 3D-printed heterogeneous radiotherapy phantoms. *Physics in Medicine & Biology*. 2019;64(21)doi:https://doi.org/10.1088/1361-6560/ab48ab

22. Tino R, Yeo A, Brandt M, Leary M, Kron T. The interlace deposition method of bone equivalent material extrusion 3D printing for imaging in radiotherapy. *Materials & Design*. 2021/02/01/ 2021;199:109439. doi:https://doi.org/10.1016/j.matdes.2020.109439

23. Aerts HJWL, Velazquez ER, Leijenaar RTH, et al. Decoding tumour phenotype by noninvasive imaging using a quantitative radiomics approach. *Nature Communications*. 2014;5:4006. doi:https://doi.org/10.1038/ncomms5006

24. Leary M, Kron T, Keller C, et al. Additive manufacture of custom radiation dosimetry phantoms: an automated method compatible with commercial polymer 3D printers. *Materials & Design*. 2015;86:487. doi:https://doi.org/10.1016/j.matdes.2015.07.052

25. Gear JI, Long C, Rushforth D, Chittenden SJ, Cummings C, Flux GD. Development of patient-specific molecular imaging phantoms using a 3D printer. *Medical physics*. 2014;41(8Part1):082502. doi:https://doi.org/10.1118/1.4887854

26. Leary M, Tino R, Keller C, et al. Additive manufacture of lung equivalent anthropomorphic phantoms: a method to control hounsfield number utilizing partial volume effect. *Journal of Engineering and Science in Medical Diagnostics and Therapy*. 2019;3doi:https://doi.org/10.1115/1.4044460

27. Ehler E, Sterling D, Higgins P. SU-C-213-01: 3D Printed Patient Specific Phantom Composed of Bone and Soft Tissue Substitute Plastics for Radiation Therapy. *Medical Physics*. 2015;42(6Part2):3188-3188. doi:https://doi.org/10.1118/1.4923782

28. Van der Walt M, Crabtree T, Albantow C. PLA as a suitable 3D printing thermoplastic for use in external beam radiotherapy. *Australasian Physical & Engineering Sciences in Medicine*. 2019/12/01 2019;42(4):1165-1176. doi:10.1007/s13246-019-00818-6

29. Kairn T, Crowe S, Markwell T. Use of 3D printed materials as tissue-equivalent phantoms. *World Congress on Medical Physics and Biomedical Engineering, June 7-12, 2015, Toronto, Canada*. 2015:728-731. doi:https://doi.org/10.1007/978-3-319-19387-8_179

30. Craft DF, Howell RM. Preparation and fabrication of a full-scale, sagittal-sliced, 3D-printed, patient-specific radiotherapy phantom. *Journal of Applied Clinical Medical Physics*. 2017;18(5):285-292. doi:https://doi.org/10.1002/acm2.12162

31. Kamomae T, Shimizu H, Nakaya T, et al. Three-dimensional printer-generated patient-specific phantom for artificial in vivo dosimetry in radiotherapy quality assurance. *Physica Medica*. 2017/12/01/ 2017;44:205-211. doi:https://doi.org/10.1016/j.ejmp.2017.10.005

32. Okkalidis N, Marinakis G. Accurate replication of soft and bone tissues with 3D printing. *Medical Physics*. 2020;47(5):2206-2211. doi:https://doi.org/10.1002/mp.14100

33. Kairn T, Zahrani M, Cassim N, Livingstone A, Charles P, Crowe S. Quasi-simultaneous 3D printing of muscle-, lung-and bone-equivalent media: a proof-of-concept study. *Physical and Engineering Sciences in Medicine*. 2020:1-10. doi:https://doi.org/10.1007/s13246-020-00864-5

34. Dancewicz OL, Sylvander SR, Markwell TS, Crowe SB, Trapp JV. Radiological properties of 3D printed materials in kilovoltage and megavoltage photon beams. *Physica Medica*. 2017/06/01/ 2017;38:111-118. doi:https://doi.org/10.1016/j.ejmp.2017.05.051

35. Park S-Y, Choi N, Choi BG, Lee DM, Jang NY. Radiological Characteristics of Materials Used in 3-Dimensional Printing with Various Infill Densities. *pmp*. 12 2019;30(4):155-159. doi:10.14316/pmp.2019.30.4.155

36. Kristiawan RB, Imaduddin F, Ariawan D, Arifin Z. A review on the fused deposition modeling (FDM) 3D printing: Filament processing, materials, and printing parameters. *Open Engineering*. 2021;11(1):639-649.

37. Soares JB, Finamor J, Silva FP, Roldo L, Cândido LH. Analysis of the influence of polylactic acid (PLA) colour on FDM 3D printing temperature and part finishing. *Rapid Prototyping Journal*. 2018;

38. Pandzic A, Hodzic D, Milovanovic A. Influence of Material Colour on Mechanical Properties of PLA Material in FDM Technology. 2019:1726-9679.

39. Wittbrodt B, Pearce JM. The effects of PLA color on material properties of 3-D printed components. *Additive Manufacturing*. 2015/10/01/ 2015;8:110-116. doi:https://doi.org/10.1016/j.addma.2015.09.006

40. Oh D, Hong C-S, Ju SG, et al. Development of patient-specific phantoms for verification of stereotactic body radiation therapy planning in patients with metallic screw fixation. *Scientific Reports*. 2017/01/19 2017;7(1):40922. doi:10.1038/srep40922

41. Retif P, Djibo Sidikou A, Letellier R, Verrecchia-Ramos E, Quetin P. Technical Note: A 3D-printed phantom for radiochromic film evaluation of moving lung tumor SBRT without dose convolution. *Medical Physics*. n/a(n/a)doi:https://doi.org/10.1002/mp.14841

42. Brock KK, Mutic S, McNutt TR, Li H, Kessler ML. Use of image registration and fusion algorithms and techniques in radiotherapy: Report of the AAPM Radiation Therapy Committee Task Group No. 132. *Medical Physics*. 2017;44(7):e43-e76. doi:https://doi.org/10.1002/mp.12256

43. Gear JI, Cummings C, Sullivan J, et al. Radioactive 3D printing for the production of molecular imaging phantoms. *Physics in Medicine & Biology*. 2020;65(17):175019. doi:https://doi.org/10.1088/1361-6560/aba40e

44. Wang S, Noh Y, Brown J, et al. Development and testing of an ultrasound-compatible cardiac phantom for interventional procedure simulation using direct three-dimensional printing. *3D Printing and Additive Manufacturing*. 2020;7(6):269-278. doi:https://doi.org/10.1089/3dp.2019.0097

45. Axford A, Dikaios N, Roberts DA, Clark CH, Evans PM. An end-to-end assessment on the accuracy of adaptive radiotherapy in an MR-linac. *Physics in Medicine & Biology*. Feb 25 2021;66(5):055021. doi:https://doi.org/10.1088/1361-6560/abe053

46. Varghese BA, Hwang D, Cen SY, et al. Identification of robust and reproducible CT-texture metrics using a customized 3D-printed texture phantom. *Journal of Applied Clinical Medical Physics*. 2021;22(2):98-107. doi:https://doi.org/10.1002/acm2.13162

Appendix

Appendix A: Gyroid structures as a lung density material

In this section, we discuss the materials and methodology utilized to illustrate the dependency of mean HU with Gyroid parameters (wall thickness, *t* and periodicity, *P*). Here, a total of fifteen gyroid phantom inserts were manufactured using ABS material (ρ = 1.09g/cm^3) (see Figure 9 and 10). The single gyroid equation was utilized to vary Gyroid parameters, as demonstrated from previous work[21]. For a baseline, an additional ED insert was manufactured using ABS with 100% infilling. CT results for printed cylindrical Gyroid ED inserts are shown in Table 4-6.

Appendix B: kV CT results from Gyroid lung sub-section, L7, containing lesion

Three identical samples of sub-section, L7, were 3D printed separately on different days using ABS filament (Raise3D Pro 2, Raise3D). 3D printed specimens were scanned in supine positions using a fan beam CT (Philips Brilliance Big Bore CT) at varied beam qualities including 140 kVp, 120 kVp, and 80 kVp (2 mm slice thickness and increments). CT results were then imported to Eclipse treatment planning system (v15.6) where separate volumetric structures were generated for the gyroid lung tissue and the cavitating lesion to extract mean HU and standard deviation (see Figure 11 and Table 7). For further comparison between different specimens within datasets, we implemented three image registrations—samples 1 to 2, samples 1 to 3, and samples 2 to 3. Due to the limited function of the treatment planning system, a maximum of two datasets were allowed for image registration. Here, we generated horizontal HU line profiles from the registered datasets—frontal, sagittal, and transversal planes (see Figure 12).

Table 1: Selected printing parameters for tissue segments using Ideamaker slicer software (Ideamaker, Raise3D, USA).

Parameters	Tissue segments			
	Gyroid lung with lesion[a]	Soft tissue[b]	Spinal cord[b]	Bone[b]
Material	ABS	PLA	PLA	Fe-PLA and PLA
Extrusion width/nozzle size [mm]	0.4	0.4	0.4	0.8 and 0.4
Layer height [mm]	0.2	0.2	0.2	0.2
No. of shells	1	1	1	1
Infill density [%]	100	100	100	100
Nozzle temperature [˚C]	255	205	205	210
Heated bed temperature [˚C]	110	60	60	60

[a]printed separately

[b]printed simultaneously using dual-extrusion printing

Table 2: kV CT results for ED phantom consisting of commercial and 3D printed phantom inserts (see Figure 5a), at 140 kVp with 2mm slice thickness and increments: their measured mean HU [± one standard deviation], measured electron density relative to water, $\rho_{e/w}$, and mass density, ρ_m are extracted using a VOI of 5 cc.

Material	Mean HU	ρ_m	$\rho_{e/w}$
Air	-930 ± 17	0.000	0.000
Lung-equivalent	-797 ± 25	0.202	0.194
ABS Gyroid[a]	-755 ± 8	0.226	0.221
Polyethylene	-55 ± 1	0.967	0.955
ABS solid	-39 ± 20	0.982	0.968
Polystyrene	-17 ± 2	0.994	0.986
Water-filled insert	11 ± 6	1.016	1.011
PLA solid	84 ± 15	1.089	1.066
Plastic water	100 ± 3	1.098	1.072
Nylon	111 ± 2	1.105	1.077
Polycarbonate	111 ± 2	1.105	1.077
Acrylic	131 ± 2	1.116	1.086
FePLA-PLA solid, V_{ratio} = 0.11[b]	283 ± 19	1.211	1.164

FePLA-PLA solid, V_{ratio} = 0.33[c]	756 ± 27	1.521	1.448
FePLA-PLA solid, V_{ratio} = 0.50[d]	1101 ± 138	1.781	1.671
Bone-equivalent	1320 ± 26	1.946	1.812
FePLA solid	2101 ± 138	2.389	2.167

[a]gyroid structure with a periodicity of 5×5×5 mm^3 and a wall thickness of 0.6 mm.

[b]material volume ratio, V_{ratio}, 0.11, corresponding to a PLA layer thickness of 1.6 mm and an Fe-PLA layer thickness of 0.2 mm.

[c]material volume ratio, V_{ratio}, 0.33, corresponding to a PLA layer thickness of 0.4 mm and an Fe-PLA layer thickness of 0.2 mm.

[d]material volume ratio, V_{ratio}, 0.50, corresponding to a PLA layer thickness of 0.2 mm and an Fe-PLA layer thickness of 0.2 mm.

Table 3: Extracted CT results from 3D printed phantom utilising the generated tissue contours (VOI from the commercial CIRS phantom dataset.

Tissue segments	Materials	Design	Mean HU	±SD
Soft tissue	PLA solid	n/a	51	139
Spinal cord			198	163
High-density bone	FePLA-PLA solid	V_{ratio} = 0.33	631	241
Low-density bone	FePLA-PLA solid	V_{ratio} = 0.11	218	97
Lung tissue	ABS Gyroid	P = 5×5×5 mm^3, t = 0.6 mm	-756	83
Lesion – tissue	ABS solid	n/a	-375	209
Lesion – cavity	n/a	n/a	-691	221

Table 4: CT results of printed cylindrical Gyroid ED inserts at 140 kVp 2/2.

P	*t*	Mean HU	±SD	Mass density (g/cm^3)
3	0.6	-598.854	10.598	0.392
4	0.6	-694.669	7.310	0.290
5	0.6	-754.726	8.627	0.226
6	0.6	-797.813	13.470	0.202
7	0.6	-827.105	24.889	0.181
3	1	-333.585	12.292	0.673
4	1	-476.643	37.615	0.522
5	1	-583.777	21.324	0.408

6	1	-662.19	23.498	0.325
7	1	-709.587	42.693	0.202
3	1.4	-185.209	18.03	0.830
4	1.4	-357.709	12.278	0.648
5	1.4	-497.139	10.923	0.501
6	1.4	-582.249	20.837	0.411
7	1.4	-636.026	43.775	0.354

Table 5: CT results of printed cylindrical Gyroid ED inserts at 120 kVp 2/2.

P	***t***	**Mean HU**	**±SD**	**Mass density (g/cm^3)**
3	0.6	-605.557	10.102	0.385
4	0.6	-700.957	7.443	0.284
5	0.6	-759.494	8.305	0.221
6	0.6	-802.948	13.661	0.201
7	0.6	-832.384	24.02	0.175
3	1	-366.436	80.145	0.650
4	1	-510.106	56.323	0.488
5	1	-629.752	96.356	0.359
6	1	-679.227	35.321	0.311
7	1	-722.723	48.48	0.259
3	1.4	-191.94	18.178	0.823
4	1.4	-363.678	11.994	0.641
5	1.4	-502.027	10.977	0.496
6	1.4	-587.008	21.001	0.405
7	1.4	-640.908	43.483	0.348

Table 6: CT results of printed cylindrical Gyroid ED inserts at 80 kVp 2/2.

P	***t***	**Mean HU**	**±SD**	**Mass density (g/cm^3)**
3	0.6	-625.285	9.799	0.366
4	0.6	-718.779	7.424	0.265
5	0.6	-776.643	7.968	0.205
6	0.6	-819.327	13.434	0.189
7	0.6	-847.981	23.106	0.155

3	1	-368.002	34.318	0.636
4	1	-498.642	51.466	0.498
5	1	-608.545	22.703	0.382
6	1	-686.492	22.551	0.299
7	1	-732.492	41.160	0.252
3	1.4	-220.088	17.657	0.794
4	1.4	-388.986	11.518	0.615
5	1.4	-525.354	10.497	0.470
6	1.4	-608.618	20.394	0.384
7	1.4	-660.983	41.595	0.327

Table 7: Mean HU (± one standard deviation) of the 3D printed Gyroid lung sub-section, L7 samples at 140 kVp, 120 kVp, and 80 kVp, 2 mm slice thickness and increments.

		Sample 1		**Sample 2**		**Sample 3**	
		lesion	**lung**	**lesion**	**lung**	**lesion**	**lung**
140 kVp	mean HU	-243.896	-765.004	-260.715	-765.372	-244.471	-764.037
	±SD	149.518	32.74	170.748	42.855	159.112	49.286
120 kVp	mean HU	-248.646	-768.199	-264.624	-767.967	-248.387	-765.972
	±SD	149.335	33.31	170.783	42.84	159.007	48.895
80 kVp	mean HU	-248.526	-773.678	-265.689	-774.025	-249.212	-772.716
	±SD	150.65	33.164	172.846	42.738	161.074	49.208

Figure 1: Design and printing workflow of an anthropomorphic phantom. 1.) generation of phantom slab 3D model, 2.) virtual post-processing of the phantom slab 3D model, 3.) application of the proposed MEX 3D printing techniques to emulate lung-, soft-, and bone-tissue densities, 4.) slicing of the phantom slab 3D model and 5.) gyroid lung sub-sections using IdeaMaker software, 6.) printing of the phantom slab and gyroid lung sub-section 3D models.

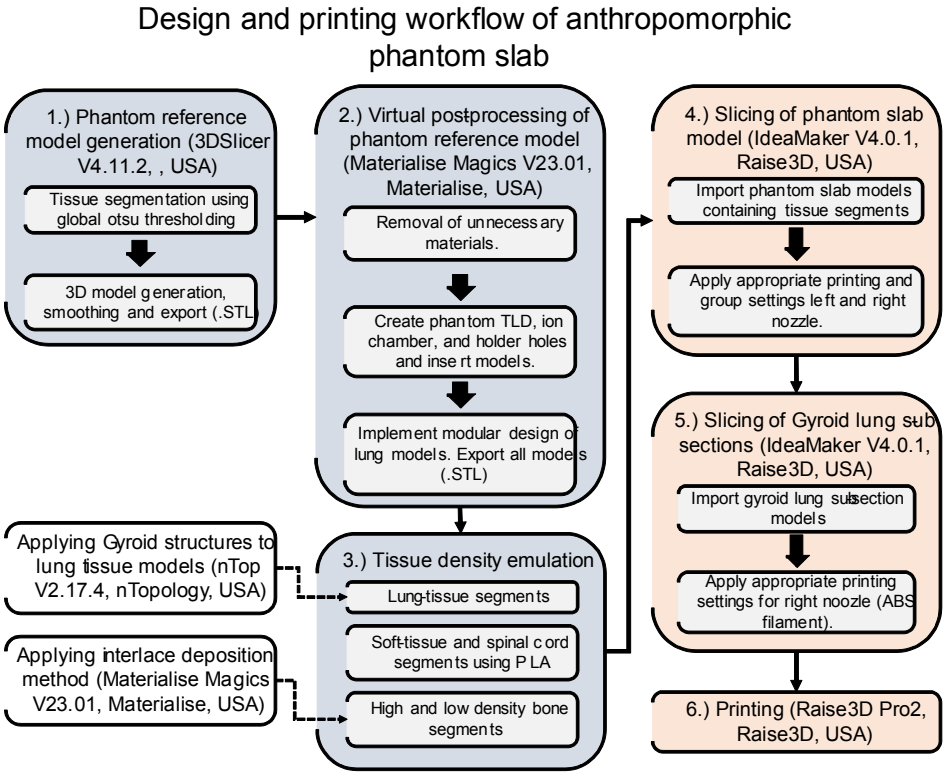

Figure 2: Segmentation and generation process of the adult CIRS ATOM phantom slab from CT for 3D printing. (a) CT of CIRS ATOM® adult phantom, (b) generated 3D phantom model with dosimetry insertion holes including holder holes for stability, TLD holders, and an ion chamber hole, (c) tissue segments including a spinal cord, high- and low- density bone, soft tissue, and lung tissue sub-sections (L1-L7 and R1-R7).

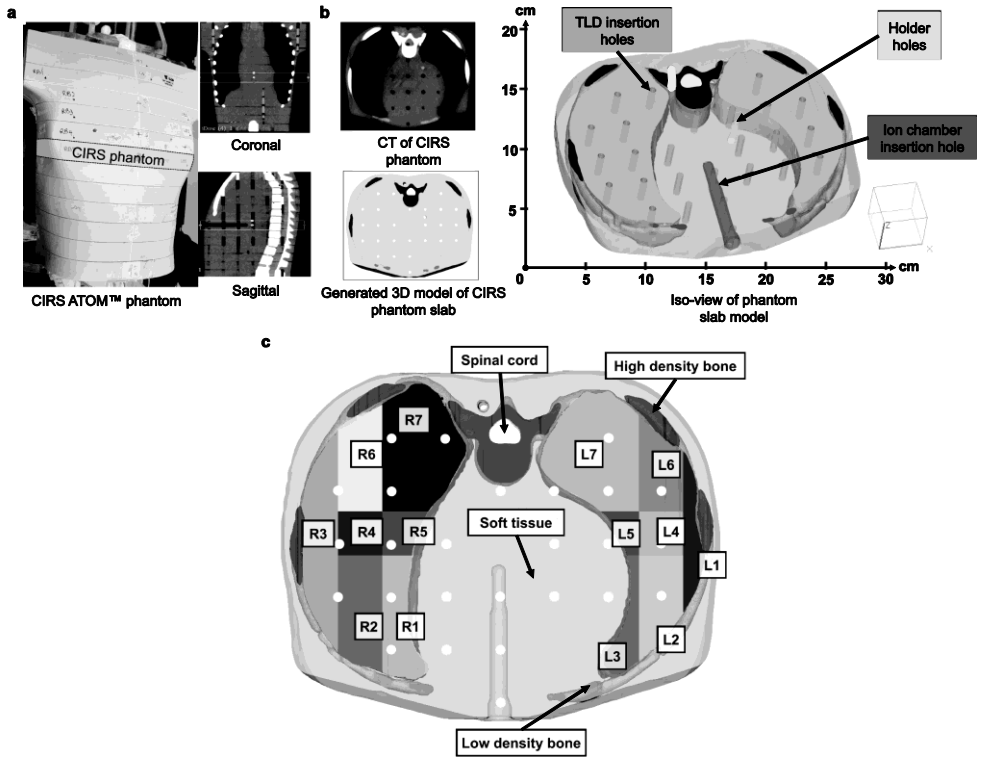

Figure 3: Generated phantom slab 3D model with a patient-specific lung lesion. (a) 3D model of the assembled phantom slab model utilizing the proposed 3D printing techniques, (b) a small spiculated lesion (squamous cell carcinoma, 5825 mm^3) with cavity (491 mm^3), positioned within the left gyroid lung sub-section, L7.

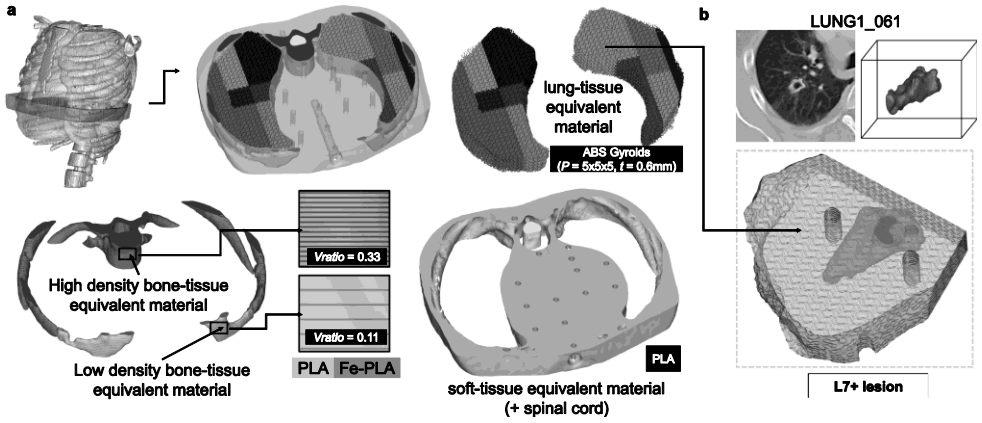

Figure 4: End-to-end testing workflow for the 3D printed anthropomorphic phantom. 1) simulation process of the 3D printed phantom using fan beam CT, 2) treatment planning process of the 3D printed phantom using Eclipse V15.6, 3) plan delivery using TrueBeam ST linear accelerator with high-definition multileaf collimator (HD-MLC), 4) and radiochromic film analysis.

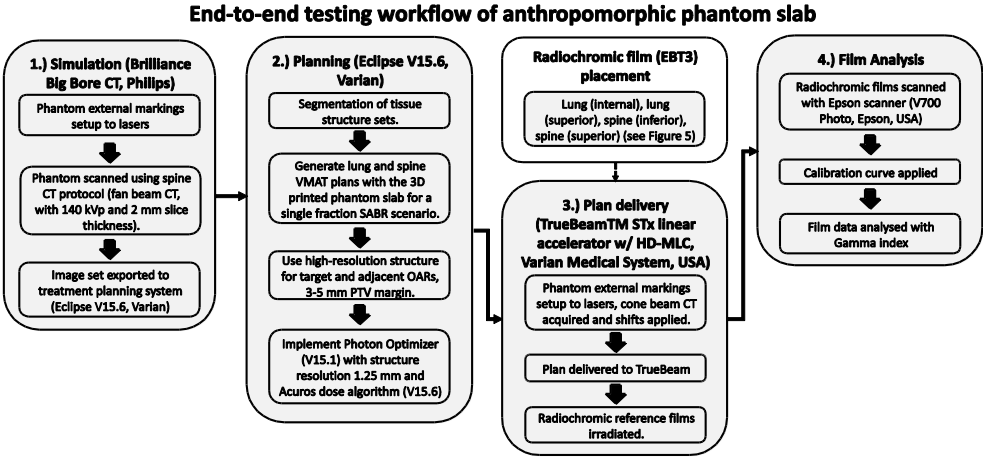

Figure 5: Manufactured phantom inserts and phantom slab. (a) CT images of the CT ED phantom containing commercial, and 3D printed phantom inserts, (b) end-to-end setup of the CIRS phantom with the 3D printed phantom. Radiochromic film placements on the 3D printed phantom include: two films for spine SABR (superior and inferior spine regions); two films for lung SABR (internal and superior lung sub-section, L7).

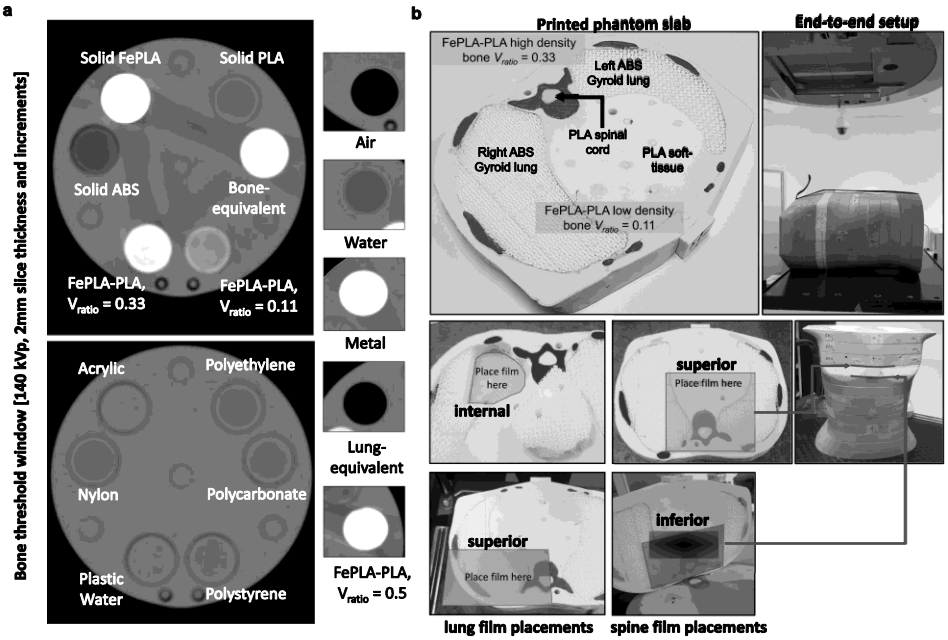

Figure 6: CT comparison of commercial CIRS Phantom and 3D printed phantom slabs. (a) alignment and scanning of phantoms, (b) drawn line profiles for CIRS phantom and the 3D printed phantom, (c) line profiles 1-5 comparing the HU of CIRS phantom and the 3D printed phantom: i, HU difference due to a missing ion chamber insert in the commercial CIRS phantom, ii, presence of high-density shells in the 3D printed phantom, iv, the limited resolution of the CT produced a slightly inaccurate representation of the 3D printed model.

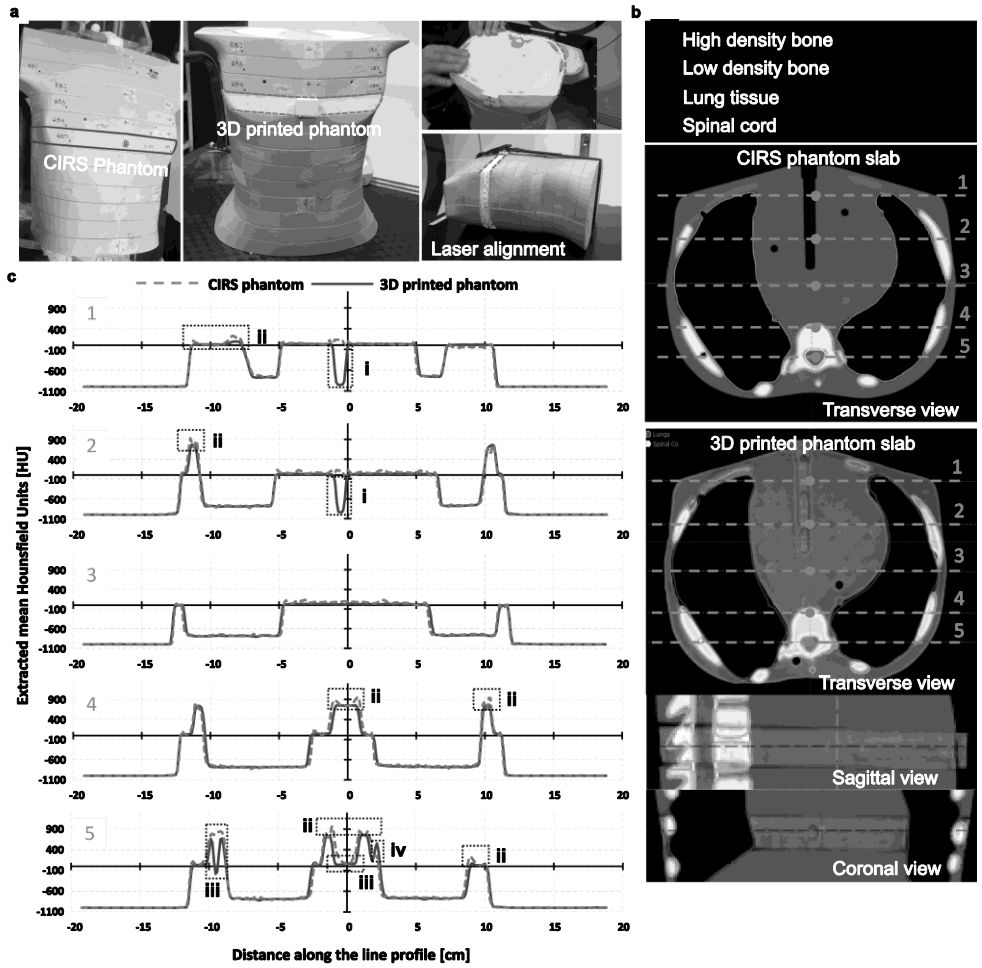

Figure 7: Comparing planned dose and film measurements of the 3D printed phantom. (a) planned isodose for lung and spine SABR (transversal) for each film positions, (b) scanned radiochromic EBT3 films, (c-d) measured isodose and gamma analysis maps, (d) generated map for global gamma criteria of 5% DD and 1 mm DTA. All geometric scales in mm. Vertical and horizontal lines were used (indicated in green) to generate line profiles for each film positions to compare planned and measured dose (see

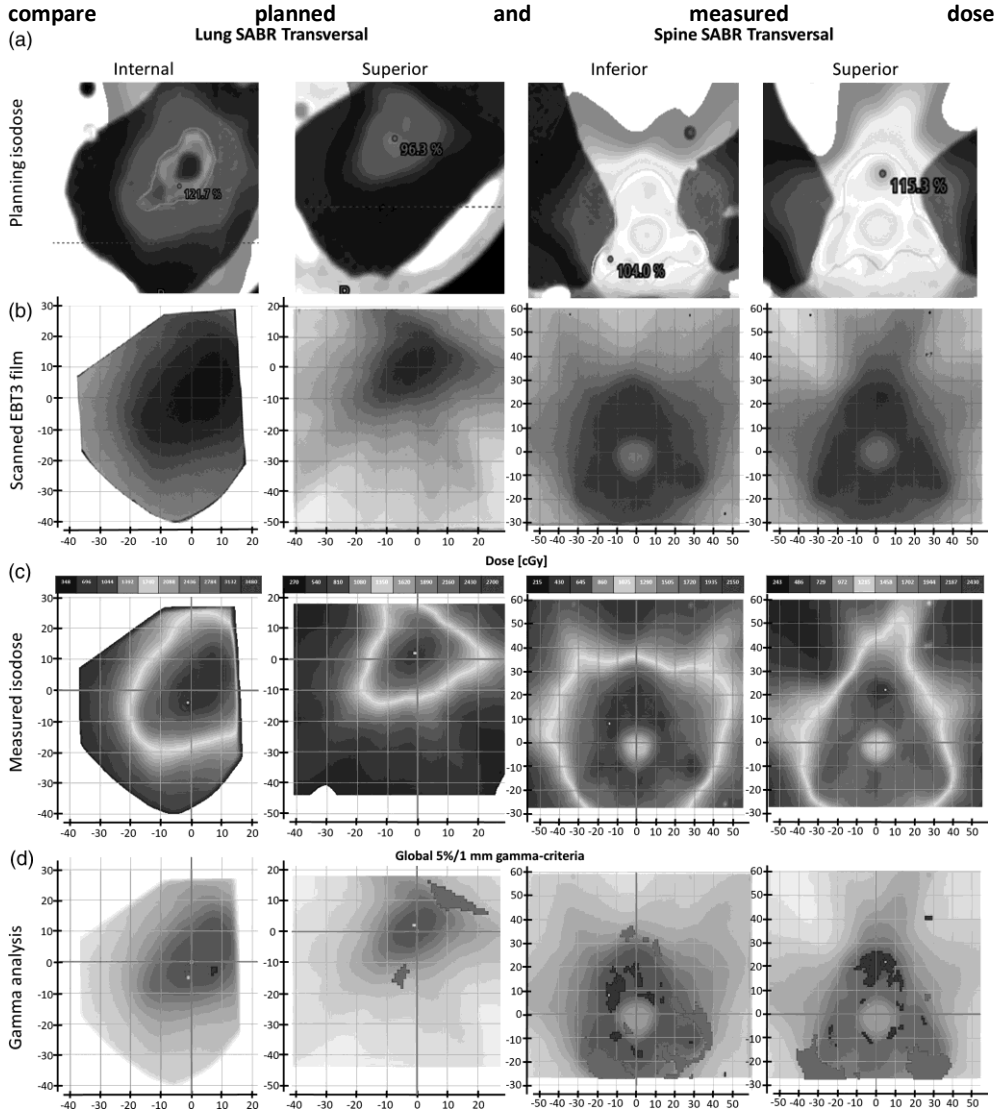

Figure 8).

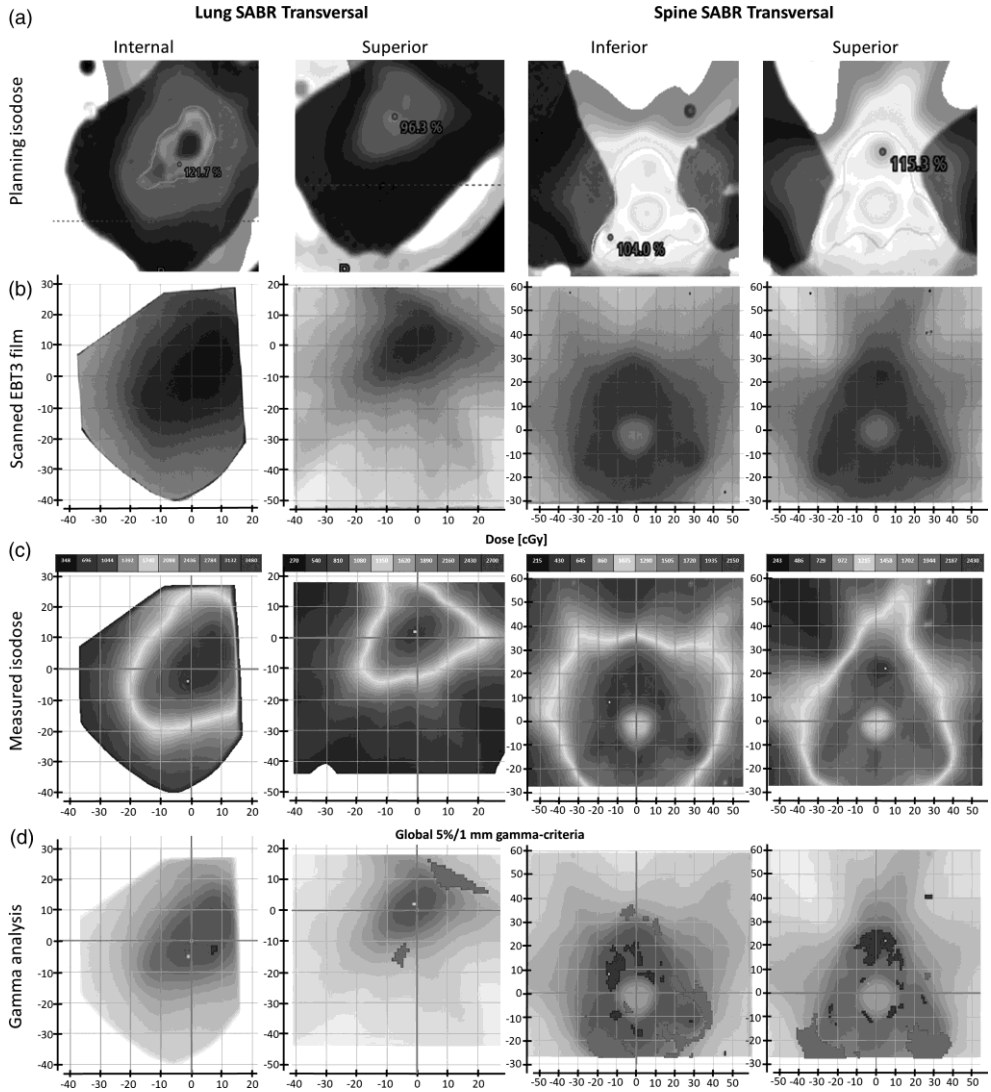

Figure 8: Generated vertical and horizontal dose profiles (cGy) from the 3D printed phantom in

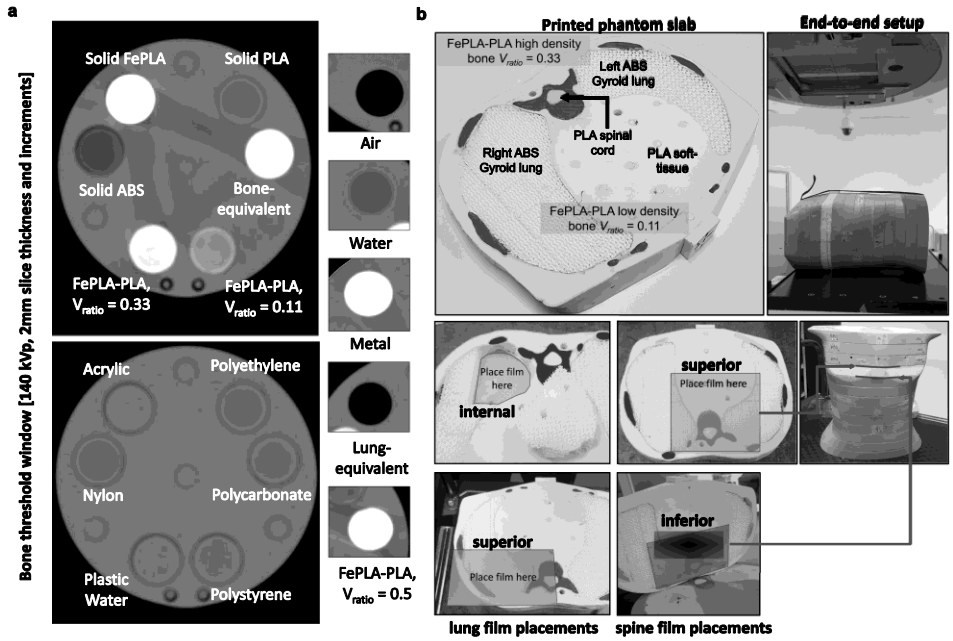

Figure 6: CT comparison of commercial CIRS Phantom and 3D printed phantom slabs. (a) alignment and scanning of phantoms, (b) drawn line profiles for CIRS phantom and the 3D printed phantom, (c) line profiles 1-5 comparing the HU of CIRS phantom and the 3D printed phantom: i, HU difference due to a missing ion chamber insert in the commercial CIRS phantom, ii, presence of high-density shells in the 3D printed phantom, iv, the limited resolution of the CT produced a slightly inaccurate representation of the 3D printed model.

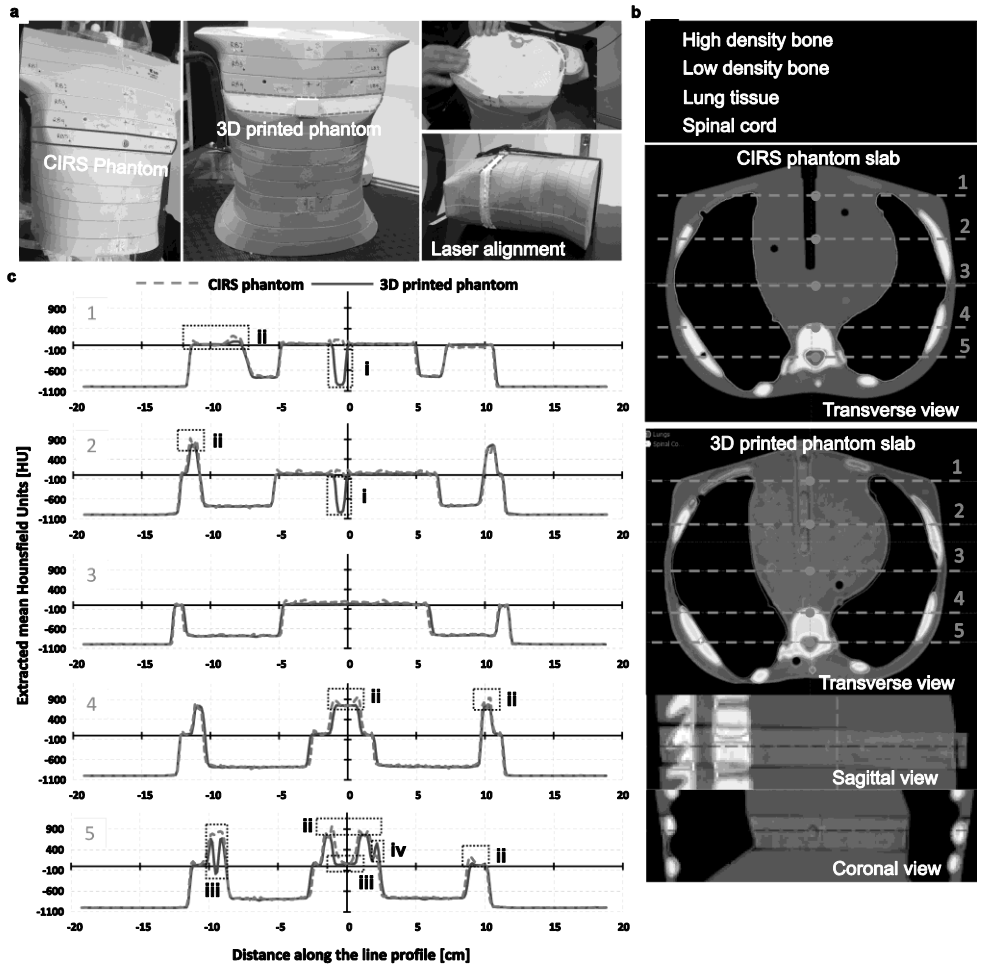

Figure 7c-d, comparing planned and measured dose attenuations for lung and spine SABR.

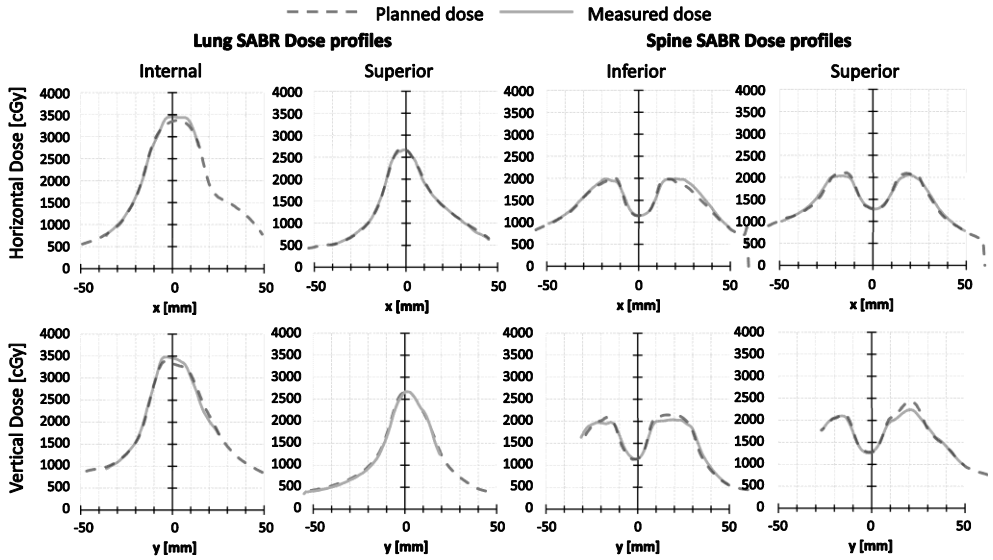

Figure 9: Parameterizing gyroid structures. (a) parameterized gyroid cube using *P* and *t*, (b) a full factorial design of experiments to investigate achievable lung-tissue like Hounsfield values with five levels of *P* and three levels of *t*, (c) specified VOI to extract HU and their standard deviation.

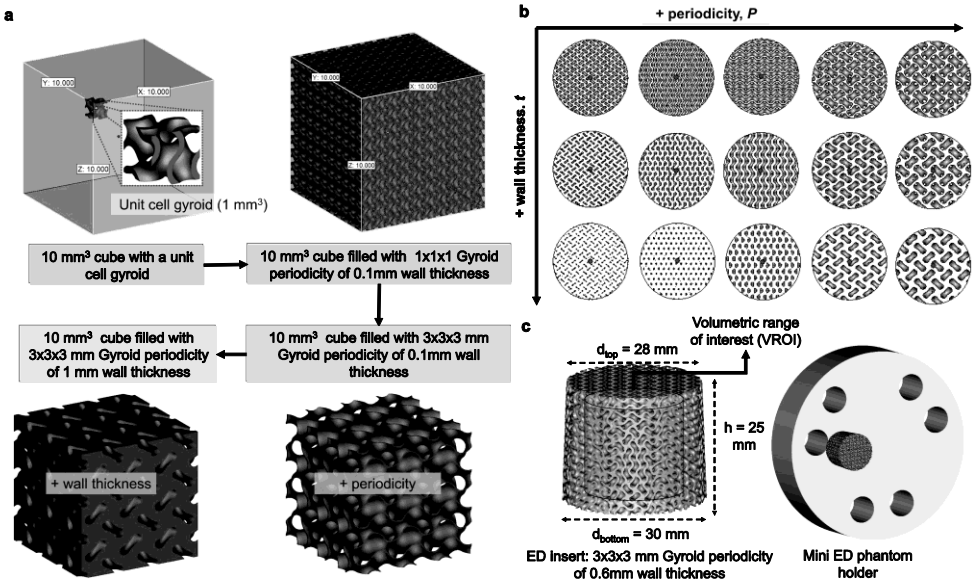

Figure 10: Printed cylindrical Gyroid ED insert CT results. (a) 140 kVp CT of printed cylindrical Gyroid ED inserts at varying wall thickness (0.6 mm, 1 mm, 1.4 mm) where a lung threshold window was used for visualization, (b) measured mean HU results of printed cylindrical Gyroid ED inserts with increasing periodicity, *P* and wall thickness, *t*, at varying kV CT energies (140 kVp, 120 kVp, 80 kVp).

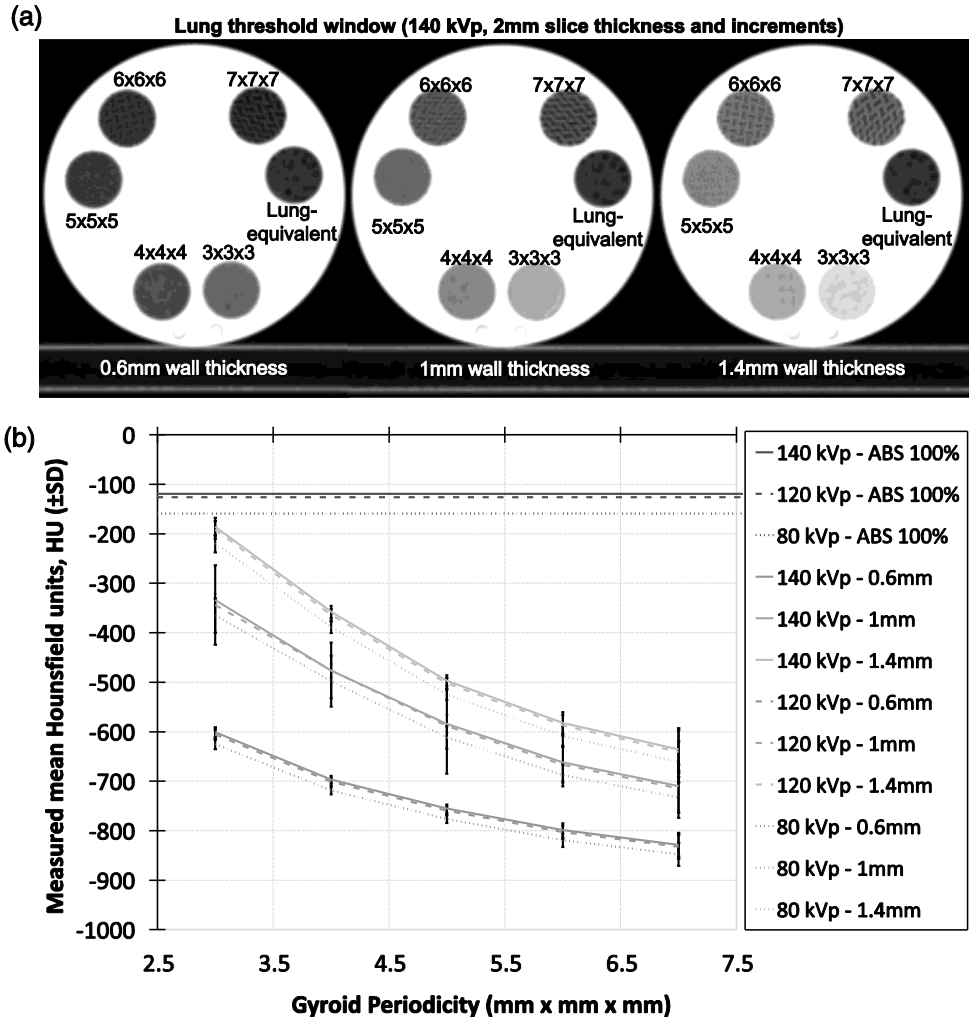

Figure 11: Generated volume structures for lesion and gyroid lung for samples 1, 2 and 3 (140 kVp, 2/2 sagittal view).

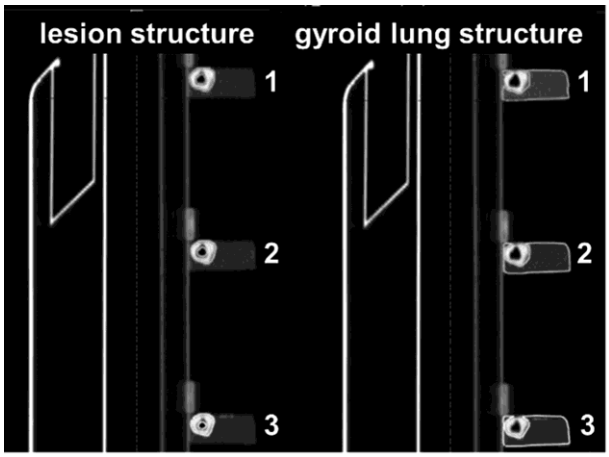

Figure 12: Generated horizontal HU line profiles from registered dataset containing samples 1, 2 and 3 (140 kVp 2/2, frontal, sagittal, and transversal planes).